Materials Transactions, Vol. 66, No. 1 (2025) pp. 1 to 16

OVERVIEW

Atomistic Model Study on Magnetic Properties of Permanent Magnets—Treatment of Thermal Fluctuation and Thermal Effects, and Future Perspective—*1

Masamichi Nishino[1],*2 and Seiji Miyashita[2]

[1] *National Institute for Materials Science, Tsukuba 305-0047, Japan*
[2] *Graduate School of Science, The University of Tokyo, Tokyo 113-0033, Japan*

We review atomistic spin model studies, a new approach for theoretical investigations, on magnetic properties of permanent magnets. In the atomistic modeling, the microscopic details of magnetic parameters and lattice structures are realistically considered, and the temperature effect, including thermal fluctuation, is properly treated based on statistical physics methods: Monte Carlo methods and stochastic Landau-Lifshitz-Gilbert equation methods. We introduce how to treat thermal effects for static and dynamical properties using these methods. Focusing especially on neodymium permanent magnets, we discuss features of magnetization, domain wall, coercivity of a grain, nucleation and pinning fields, and dysprosium substitution effect, which were first elucidated with those methods. [doi:10.2320/matertrans.MT-M2024132]

(Received August 28, 2024; Accepted October 28, 2024; Published December 25, 2024)

Keywords: *atomistic spin model, thermal fluctuation, thermal effects, permanent magnets, stochastic Landau-Lifshitz-Gilbert (LLG) equation, Monte Carlo method*

1. Introduction

The control of the coercive force (coercive field) of permanent magnets is an important issue for achieving high energy conversion efficiency. Neodymium magnets (Nd-Fe-B magnets) [1–9] are known as powerful permanent magnets and used in motors, generators, electrical appliances, etc. Their application is expected to expand in the future due to the growing demand for electric vehicle motors. Neodymium magnets have a problem with coercivity at high temperatures and are often reinforced by adding heavy rare earths such as dysprosium (Dy). Japan depends on foreign countries for the rare earth resources, but due to price instability, etc., development of high-performance permanent magnets with reduced use of rare elements is required.

Against this background, the Elements Strategy Initiative Center for Magnetic Materials (ESICMM) project (2012–2021), a national project based at National Institute for Materials Science (NIMS), has been carried out for 10 years since 2012, and coercivity research has made significant progress in both experimental and theoretical aspects [10]. In this review, we mainly focus on the microscopic modeling based on the electron theory and theoretical studies on the coercivity at finite temperatures which were developed by the authors and collaborators in ESICMM [11–28].

Theoretical studies of the magnetic properties and coercive force of permanent magnets have been developed in the field of micromagnetics [29]. For details of micromagnetics simulations, please refer to the review by Tomohiro Tanaka in the same special issue. In micromagnetics simulations, a continuum model in which the magnetization is spatially continuous with nm-order block magnetization (fixed magnitude of magnetization) as the smallest unit is considered, and magnetic materials are described with a small number of macroscopic magnetic parameters, mainly exchange stiffness constant (A) and magnetic anisotropy energy (K). This method has the advantage that the system (the size is on the order of μm) of the aggregate of grains constituting a magnetic material can be treated, and many simulations of magnetic properties such as magnetization reversal have been carried out. However, due to the coarse graining of the model, the microscopic mechanism of the magnetic properties induced by atomic-scale magnetic interactions cannot be treated. In addition, there is a problem in handling thermal fluctuations and temperature effects, as described below.

Coercivity at finite temperatures is a phenomenon that involves the collapse of a metastable magnetic state due to thermal activation. The magnetization reversal is a stochastic process, since it requires crossing the energy barrier and is caused by thermal fluctuations. In order to study such effects quantitatively, it is necessary to treat entropy effects at temperature T correctly according to statistical mechanics. In thermal equilibrium, using the energy $E(i)$ of state i, the probability of realization of state i, $P_{\mathrm{eq}}(i)$, in the canonical ensemble is expressed as

$$P_{\mathrm{eq}} = \frac{1}{Z} e^{-\beta E(i)}. \tag{1}$$

Here, β is defined by $\beta = \frac{1}{k_{\mathrm{B}}T}$ using the Boltzmann constant k_{B}. Z is a quantity called the partition function and defined by

$$Z = \sum_{i}^{\mathrm{all}} e^{-\beta E(i)}. \tag{2}$$

The sum is taken for all states. Thus, the value of the thermal equilibrium state $\langle A \rangle$ of any physical quantity A is given by the average in the canonical ensemble as follows

$$\langle A \rangle = \frac{1}{Z} \sum_{i}^{\mathrm{all}} A(i) e^{-\beta E(i)}. \tag{3}$$

When using the coarse-grained Hamiltonian for the continuum model of micromagnetics, the degrees of freedom (entropy) of the states are unclear and it is difficult to apply the above probabilities. In order to properly handle temper-

---

[*1] This Paper was Originally Published in Japanese in J. Japan Inst. Met. Mater. **87** (2023) 158–172.

[*2] Corresponding author, E-mail: nishino.masamichi@nims.go.jp

ature effects, it is necessary to use statistical mechanics methods with the canonical ensemble. By constructing a spin model based on atomistic theory that takes into account the spin of all atoms in the system, the state and number of states (entropy) can be defined, and statistical mechanics methods can be used to correctly incorporate temperature effects in the analysis. In this paper, we will focus on neodymium magnets in particular, explain the atomistic spin model, and introduce statistical mechanics methods for calculating magnetic properties at finite temperatures (including absolute zero). Various magnetic properties revealed by using the methodologies will be discussed.

2. Atomistic Spin Model

The unit cell of $Nd_2Fe_{14}B$, the hard magnet phase of neodymium magnets, is shown in Fig. 1 [30]. There are two types of Nd sites, six types of Fe sites and one type of B site. We adopt the following atomistic Hamiltonian as a microscopic model for neodymium magnets [13–15, 24]. This system is a three-dimensional ferromagnet, and we treat the spins classically.

$$\mathcal{H} = -\sum_{i<j} 2J_{ij}\boldsymbol{s}_i \cdot \boldsymbol{s}_j - \sum_{i}^{\mathrm{Fe}} D_i (s_i^z)^2 \\ + \sum_{i}^{\mathrm{Nd}} \sum_{l,m} \Theta_{l,i} A_{l,i}^m \langle r^l \rangle_i \hat{O}_{l,i}^m - h \sum_i S_i^z. \qquad (4)$$

J_{ij} is the exchange interaction between the ith and jth atoms and D_i is the anisotropy energy of the ith Fe atom. The third term is the crystal electric field (CEF) energy of Nd, where $\Theta_{l,i}$, $A_{l,i}^m$, $\langle r^l \rangle_i$ and $\hat{O}_{l,i}^m$ are the Stevens factor, coefficient of the spherical harmonics of the crystalline electric field, average of r^l over the radial wave function, and Stevens operator, respectively. The fourth term is the Zeeman term, where h is the external magnetic field. We consider $l = 2, 4, 6$ and $m = 0$ (diagonal terms). $\hat{O}_{l,i}^m$ is expressed as $\hat{O}_2^0 = 3J_z^2 - J^2$, etc.

For Fe and B atoms, $\boldsymbol{s}_i$ denotes the magnetic moment of the i-th site, whereas for Nd, $\boldsymbol{s}_i$ is the moment of the valence electrons (5d and 6s) and strongly coupled to the moment of the 4-f electrons, $\boldsymbol{\mathcal{J}}_i = g_{\mathrm{T}}\boldsymbol{J}_i\mu_{\mathrm{B}}$ through the Hund coupling as shown in Fig. 2(a). Here, g_{T} is Landé g-factor and $\boldsymbol{J}_i$ is the total angular momentum consisting of the orbital angular momentum $\boldsymbol{\mathcal{L}}$ and the spin angular momentum $\boldsymbol{\mathcal{S}}$. $J = \mathcal{L} - \mathcal{S} = 9/2$ and $g_{\mathrm{T}} = 8/11$. Therefore, the total moment of Nd atoms is $\boldsymbol{S}_i = \boldsymbol{s}_i + \boldsymbol{\mathcal{J}}_i$. For Fe and B atoms, we define $\boldsymbol{S}_i = \boldsymbol{s}_i$. Note that $\boldsymbol{s}_i$ of a Nd atom and $\boldsymbol{S}_i$ $(= \boldsymbol{s}_i)$ of an Fe atom are antiferromagnetically coupled, while $\boldsymbol{S}_i$ of a Nd atom and $\boldsymbol{S}_i$ of an Fe atom are ferromagnetically coupled.

We used the magnetic moments and exchange interactions estimated by Korringa-Kohn-Rostoker (KKR) [31] ab initio calculations. The values are given in Ref. [24]. $Nd_2Fe_{14}B$ has itinerant electrons, but no methodology has been established to incorporate the effect of itinerant magnetism. Here, we assumed that J_{ij} is widely distributed with respect to the distance due to the itinerancy. We then considered J_{ij} in the range of $r = 3.52$ Å, where the contribution to the magnetic interactions is large [13]. For the anisotropy of Fe, we adopt the literature values estimated by a first-principles calculation [32]. For Nd atoms, the first-principles estimates of the crystal field coefficients $A_{l,i}^m$ are not yet established, so we adopted the experimental estimates [33], and for $\langle r^l \rangle_i$ we used the values of a Hartree-Fock calculation [34]. For the system size treated in this review (less than a few tens of nm scale), the magnetic dipole interaction is not so important and was not considered here, but its treatment will be discussed in chapter 8.

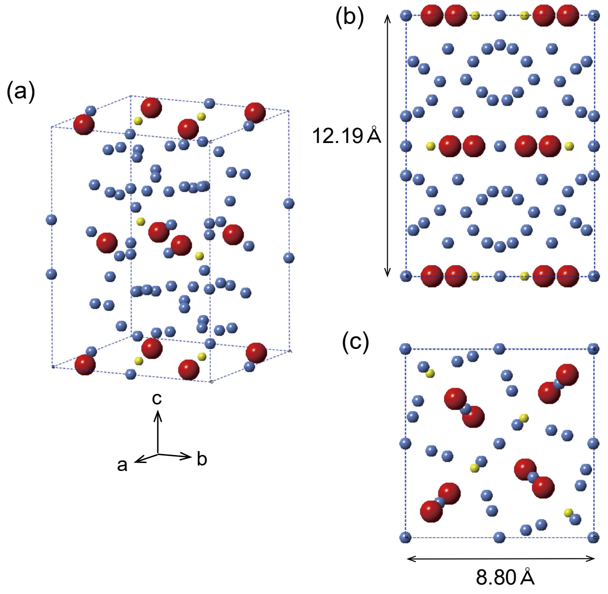

Fig. 1 (a) Unit cell of $Nd_2Fe_{14}B$. Nd, Fe, and B atoms are denoted by red, blue, and yellow spheres, respectively. The lattice constants for the a, b, and c axes are $d_a = d_b = 8.80$ Å, and $d_c = 12.19$ Å, respectively. (b) Side view (from a or b axis). (c) Top view (from c axis). Reprinted figure with permission from [M. Nishino *et al.*, Phys. Rev. B 103, 014418 (2021)]. Copyright (2021) by the American Physical Society. (online color)

3. Computational Methods for Thermodynamic Quantities and Dynamics

If an atomistic spin model such as eq. (4) is constructed, the states and number of states of the system can be clearly defined, and finite temperature properties can be calculated using statistical mechanics methods. Here we mainly describe Monte Carlo methods used to calculate thermal equilibrium states, and the stochastic Landau-Lifshitz-Gilbert (sLLG) equation [11, 35] used to calculate time-dependent dynamics.

3.1 Monte Carlo method

3.1.1 Canonical ensemble Monte Carlo method

Monte Carlo methods are often used to calculate the physical quantity $\langle A \rangle$ in thermal equilibrium. In Monte Carlo methods, the eq. (3) is realized by sampling with a probability dependent on the state i (importance sampling) and taking the sampling average. Let the spin state $(\boldsymbol{S}_1 \cdots \boldsymbol{S}_k \cdots \boldsymbol{S}_N)$ be the state i at time t, then the probability of state i at $t + \Delta t$ is given by the following master equation

$$P(i, t + \Delta t) = P(i, t) - \sum_{j \neq i} W(i \to j)\Delta t P(i, t) \\ + \sum_{j \neq i} W(j \to i)\Delta t P(j, t). \qquad (5)$$

Here, $W(i \to j)$ is the transition probability per unit time from

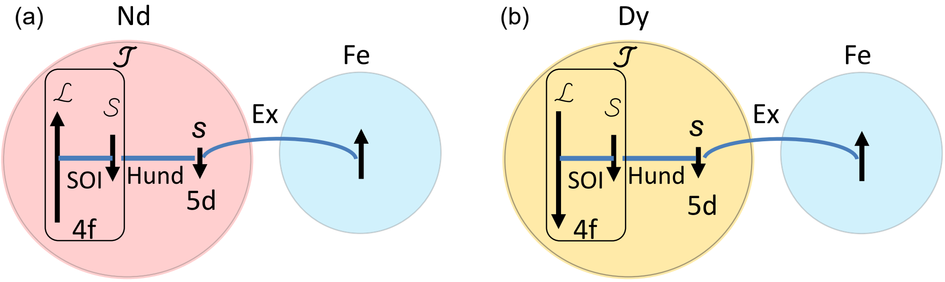

Fig. 2 (a) Magnetic coupling between Nd and Fe atoms. The total moment in an Nd atom and that in an Fe atom are ferromagnetically coupled. Ex and SOI represent the exchange interaction and spin-orbit interaction, respectively. (b) Magnetic coupling between Dy and Fe atoms. The total magnetic moment of a Dy atom and that of an Fe atom are antiferromagnetically coupled. Reprinted figure with permission from [M. Nishino *et al.*, Phys. Rev. B 106, 054422 (2022)]. Copyright (2022) by the American Physical Society. (online color)

state i to state j. In Monte Carlo methods, the state is updated every one step (one Monte Carlo step) with $\Delta t = 1$. If the following ergodicity and detail balance are satisfied for the transition probability $W(i \to j)$ for any states i, j, then starting from any initial state, convergence to a unique stationary state is guaranteed, generating an equilibrium distribution (canonical distribution).

(I) Ergodicity (connectivity condition): for any states i, j, the transition probability $W(i \to j)$ is non-zero, or can be expressed as the product of a finite number of non-zero transition probabilities.

(II) Detailed balance (this is a sufficient conditions and there are some methods which do not satisfy the detailed balance [36]):

$$P(i)_{\text{eq}} W(i \to j) = P(j)_{\text{eq}} W(j \to i). \tag{6}$$

Let $P(i)_{\text{eq}} = e^{-\beta E(i)}/Z$ (equilibrium distribution). In the Metropolis algorithm, which is often used to practice these conditions, the state update of $i \to j$ is performed with the probability $W(i \to j) = 1$ for $\mathcal{H}(i) \geq \mathcal{H}(j)$ and $W(i \to j) = \exp(-\beta(\mathcal{H}(j) - \mathcal{H}(i)))$ for $\mathcal{H}(i) < \mathcal{H}(j)$. The transition probabilities can be chosen arbitrarily if (I) and (II) are satisfied. Since the Monte Carlo step is different from real time, Monte Carlo methods are used for the calculation of physical quantities in equilibrium and of the free energy as shown in Sec. 3.1.2, while the method described in Sec. 3.2 is used for the analysis of real time dynamics.

3.1.2 Generalized ensemble methods and free energy calculations

The partition function can also be expressed using the density of states $\Omega(E)$ with respect to energy as

$$Z = \sum_{E} \Omega(E) e^{-\beta E}. \tag{7}$$

Once the density of states is known, the partition function is obtained and the free energy F can be calculated by the following equation.

$$F = -\frac{1}{\beta} \ln Z. \tag{8}$$

Using the multi-canonical Monte Carlo method [37, 38] it is possible to calculate the free energy.

In the canonical ensemble Monte Carlo method just described, the sampling is based on the Boltzmann factor $e^{-\beta E}$. In this sampling, the states near a high energy barrier have low probabilities of realization $P(E)$ ($\propto e^{-\beta E}$) and are not sampled well. Therefore, the energy histogram $H(E) \propto \Omega(E)P(E) \propto \Omega(E)e^{-\beta E}$ is close to zero for energies near high barriers. The multicanonical method samples by a non-Boltzmann factor $e^{-f(E)}$ so that high energy states are also sampled. The probability of realization $P(E)$ is adjusted so that the energy histogram $H(E)$ is flat ($H(E) = C$(constant)), and finally a random walk on the energy space is realized to obtain $P(E) \simeq \frac{C}{\Omega(E)}$. When $\Omega(E)/C$ is obtained, the free energy can be calculated from the eqs. (7) and (8) (where C is the contribution of constant). This method is more laborious than canonical ensemble Monte Carlo methods, but the Wang-Landau method [38], which is a kind of the multi-canonical method, is often used. The multi-canonical method and the replica exchange method that takes into account transitions between different temperatures [39], etc., are called generalized ensemble methods. These methods were developed for the calculation of first-order transitions and for the calculation of global minima in systems with multi-valley structures of potential energy, and are used in various fields such as spin glass relaxation and protein structure calculations.

In coercive force (field) analysis, it is convenient to consider the probability of realization in the magnetization space. Using the density of states as a function of energy and magnetization M_z, the partition function is expressed as

$$Z = \sum_{M_z} \sum_{E} \Omega(E, M_z) e^{-\beta E} \equiv \sum_{M_z} Z(M_z). \tag{9}$$

With the formula

$$F(M_z) = -\frac{1}{\beta} \ln Z(M_z), \tag{10}$$

the free energy in the magnetization space (free energy landscape) can be calculated, and the energy barrier as a function of magnetization can be obtained. Here, the histogram $H(M_z)$ for magnetization is $H(M_z) \propto Z(M_z)$ in the canonical ensemble, but $H(M_z) \propto Z(M_z)P(M_z)$ in the multi-canonical method, and the probability of realization of magnetization $P(M_z)$ is adjusted so that $H(M_z) = C$ as in the energy case [40, 41]. Finally, $P(M_z) = C/Z(M_z)$ is obtained, and $F(M_z)$ is obtained from the formula (10).

3.2 Stochastic LLG equation method

The Monte Carlo method is an effective method for calculating zero-temperature or finite-temperature equilibrium states, but it does not provide concrete information on real-time dynamics, such as what the state will be after a certain number of seconds. For real-time dynamics, it is necessary to solve the equations of motion for spins. The LLG equation (eq. (11)) is a standard equation, which consists of the equation of motion of the torque representing the precession motion of the magnetization and its relaxation terms.

$$\frac{\mathrm{d}}{\mathrm{d}t}\boldsymbol{S}_i = -\frac{\gamma}{1+\alpha_i^2}\boldsymbol{S}_i \times \boldsymbol{h}_i^{\mathrm{eff}} - \frac{\alpha_i\gamma}{(1+\alpha_i^2)S_i}\boldsymbol{S}_i \times [\boldsymbol{S}_i \times \boldsymbol{h}_i^{\mathrm{eff}}]. \tag{11}$$

Here, γ is the electron gyromagnetic ratio and α_i is the damping constant.

$$\boldsymbol{h}_i^{\mathrm{eff}} = -\frac{\partial\mathcal{H}}{\partial\boldsymbol{S}_i} \tag{12}$$

is the effective magnetic field applied to the i-site, including the external magnetic field, exchange interactions and dipole interactions around the i-site, and magnetic field due to the magnetic anisotropy energy of the i-site.

At absolute zero temperature, there are no processes crossing the energy barrier because there are no thermal fluctuations, and the dynamics of magnetization can be calculated using this equation. In contrast, in the finite temperature case, thermal fluctuations can cause a relaxation process from a metastable state to a stable state crossing the energy barrier. The effect of thermal fluctuations is given by introducing a noise field $\boldsymbol{\xi}_i(t)$ [11, 35]. $\boldsymbol{h}_i^{\mathrm{eff}}$ is modified as follows.

$$\boldsymbol{h}_i^{\mathrm{eff}} = -\frac{\partial\mathcal{H}}{\partial\boldsymbol{S}_i} + \boldsymbol{\xi}_i(t). \tag{13}$$

Here, $\boldsymbol{\xi}_i(t) = (\xi_i^x, \xi_i^y, \xi_i^z)$ is the white Gaussian noise and satisfies the following relations

$$\langle\xi_i^\mu(t)\rangle = 0, \quad \langle\xi_i^\mu(t)\xi_j^\nu(s)\rangle = 2\mathcal{D}_i\delta_{ij}\delta_{\mu\nu}\delta(t-s). \tag{14}$$

This noise is related to temperature as shown below. The time evolution equation of the probability distribution function equivalent to this sLLG equation (Stratonovich representation of the Fokker-Planck equation) [11] is given by

$$\begin{aligned}\frac{\partial}{\partial t}P(\boldsymbol{S}_1,\cdots,\boldsymbol{S}_N,t) &= \sum_i \frac{\gamma}{1+\alpha_i^2}\frac{\partial}{\partial\boldsymbol{S}_i}\cdot\left\{\left[\frac{\alpha_i}{S_i}\boldsymbol{S}_i\times(\boldsymbol{S}_i\times\boldsymbol{H}_i^{\mathrm{eff}})\right.\right.\\ &\left.\left.-\gamma D_i\boldsymbol{S}_i\times\left(\boldsymbol{S}_i\times\frac{\partial}{\partial\boldsymbol{S}_i}\right)\right]P(\boldsymbol{S}_1,\cdots,\boldsymbol{S}_N,t)\right\}\\ &+\sum_i\frac{\gamma}{1+\alpha_i^2}(\boldsymbol{S}_i\times\boldsymbol{H}_i^{\mathrm{eff}})\cdot\frac{\partial}{\partial\boldsymbol{S}_i}P(\boldsymbol{S}_1,\cdots,\boldsymbol{S}_N,t).\end{aligned} \tag{15}$$

Now, if the following fluctuation-dissipation relation is satisfied

$$\mathcal{D}_i = \frac{\alpha_i k_{\mathrm{B}}T}{\gamma S_i}, \tag{16}$$

it can be proved that the distribution function in the steady state ($t \to \infty$) at temperature T corresponds to the canonical distribution [11, 35]

$$P_{\mathrm{eq}}(\boldsymbol{S}_1,\cdots,\boldsymbol{S}_N) \propto \exp(-\beta\mathcal{H}(\boldsymbol{S}_1,\cdots,\boldsymbol{S}_N)). \tag{17}$$

That is, given a damping constant, the temperature T can be controlled by changing the magnitude (amplitude) of the noise. The sLLG equation is a stochastic differential equation, and since the noise is multiplied by the physical quantity (magnetization), it is a so-called multiplicative process, and care must be taken in the method of integration.

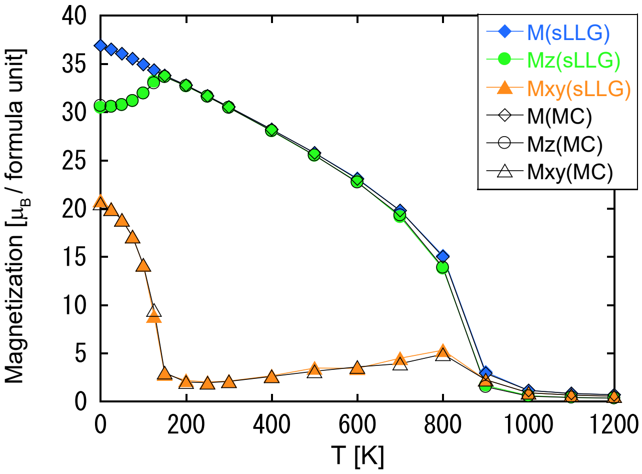

Fig. 3 Temperature dependences of M, M_z, and M_{xy} of the atomistic model for the $\mathrm{Nd_2Fe_{14}B}$ magnet with comparison between Monte Carlo and stochastic-LLG methods. $6 \times 6 \times 6$ unit cells with periodic boundary conditions. (online color)

4. Thermodynamic Properties

4.1 Magnetization

Figure 3 shows the temperature dependence of magnetizations of $\mathrm{Nd_2Fe_{14}B}$ magnets in equilibrium, calculated by the sLLG and Monte Carlo methods (Metropolis algorithm). M is the magnitude of magnetization, M_z is the z component of magnetization (c-axis component), and M_{xy} is the xy component of magnetization (ab-plane component). The calculated values of the sLLG equation and those of the Monte Carlo method are in good agreement, and the equilibrium state (canonical distribution) is realized in the calculations with both methods.

The spin-reorientation transition is confirmed by simulations to occur around 150 K, where M_z has a maximum [4, 6–8]. Figure 4(a) illustrates the temperature dependence of the crystal electric field (CEF) energy of Nd atoms in $\mathrm{Nd_2Fe_{14}B}$. θ is the angle from the c-axis. At absolute zero temperature, the potential minimum exists at $\theta \simeq 0.2\pi$ and $\theta \simeq 0.8\pi$, but above the spin-reorientation transition temperature, the minimum shifts to $\theta = 0$ and $\theta = \pi$, and it is understood that the spin-reorientation transition occurs.

The Curie temperature T_{C} is about 870 K (the estimated value of T_{C} for the infinite system by Binder plot [42]), which overestimates the experimental value of about 600 K [4, 5]. This is due to the overestimation of the magnetic interactions in the first-principles calculation. However, considering the current accuracy of first-principles calculations, it is a sufficiently reliable value. Therefore, we will henceforth express temperature in units of T_{C}. In our experience, for obtaining physical quantities in equilibrium, the Monte Carlo method requires shorter simulation time.

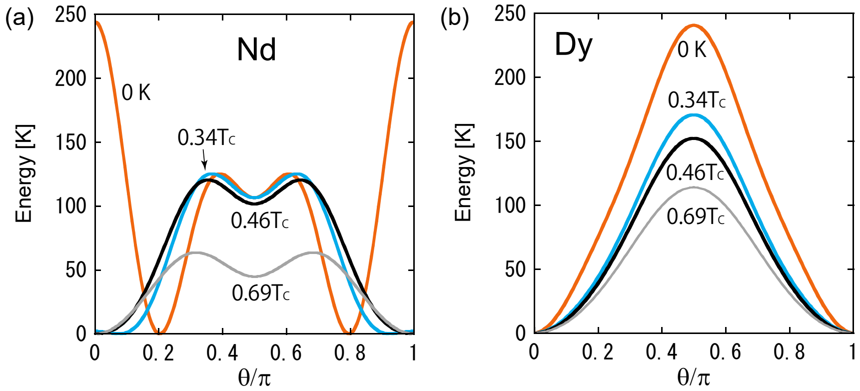

Fig. 4 Crystal electric field energy (a) for a Nd atom and (b) for a Dy atom as a function of θ at zero and finite temperatures. Reprinted figure with permission from [M. Nishino *et al.*, Phys. Rev. B 106, 054422 (2022)]. Copyright (2022) by the American Physical Society. (online color)

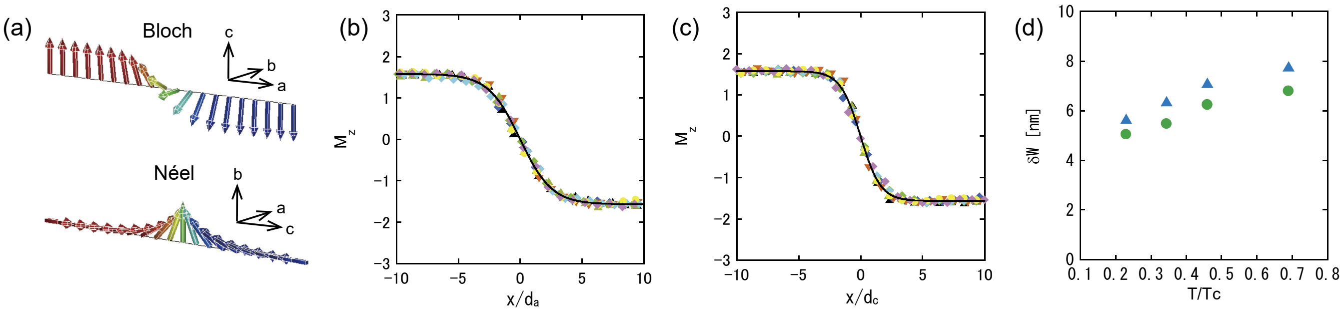

Fig. 5 (a) Bloch-type wall and Néel-type wall. (b) M_z along *a*-axis (Bloch-type) at $0.46T_C$. The unit of the vertical axis is μ_B/atom. The functions $m_z(x)$ is given by a solid line. Here symbols denote $M_z(x)$ at different MC steps. (c) M_z along *c*-axis (Néel-type) at $0.46T_C$. (d) Temperature variation of δW for Bloch-type (triangles) and Néel-type (circles) walls. Reprinted figure with permission from [M. Nishino *et al.*, Phys. Rev. B 95, 094429 (2017)]. Copyright (2017) by the American Physical Society. (online color)

4.2 Domain wall

The properties of domain walls are important in the study of the magnetization reversal process. In this section, we show the variation of the domain wall shape and width with temperature calculated by the Monte Carlo method (Metropolis method). Since neodymium magnets have anisotropy along the *c*-axis, two types of domain walls are possible, as shown in Fig. 5(a). One is a Bloch-type domain wall that moves along the *a*-axis (or *b*-axis), and the other is a Néel-type domain wall that moves along the *c*-axis. Regarding the domain walls of Bloch and Néel, the magnetization $\{M_z(x)\}$ at position x in the *a*-axis and *c*-axis, respectively, was calculated by the Monte Carlo method, and superimositions of the obtained snapshots (symbols) are shown in Fig. 5(b) and Fig. 5(c) [14]. The abscissa is in units of the lattice constant. Next, from these plots, we obtained the domain wall width. The domain wall width is defined in the continuum model as follows [29]. Let $m(T)$ be the magnitude of magnetization at temperature T, the z component of magnetization at position x from the center of the domain wall ($m_x(x) = 0$) is

$$m_z(x) = -m(T)\tanh\left(\frac{x}{\delta_0}\right). \tag{18}$$

δ_0 is called the wall parameter and is defined by $\delta_0 \equiv \sqrt{\frac{A}{K_1}}$, where A and K_1 are the stiffness constant and the first magnetic anisotropy constant, respectively, of the continuum model. The domain wall width is given by

$$\delta W = \pi\delta_0 = \pi\sqrt{\frac{A}{K_1}}. \tag{19}$$

By fitting $m_z(x)$ (eq. (18)) with δ_0 and $m(T)$ as fitting parameters to the snapshot data of M_z obtained by the Monte Carlo method, δ_0 is obtained and the domain wall width δW can be evaluated. The temperature dependence of the domain wall width is given in Fig. 5(d). At high temperatures, the domain wall broadens. At around room temperature, it is about 6–7 nm. The domain wall widths estimated by experiments for A and K_1 [29, 43, 44] are 3.6–5.4 nm, and those observed by electron microscopy [45–47] are 1–10 nm. The calculated values are close to the experimental ones.

The fact of the narrower width of the Néel wall than that of the Bloch wall is considered to be due to the lattice structure in which the Nd surface is perpendicular to the *c*-axis. The exchange interactions between adjacent Nd and Fe atoms are smaller than those between adjacent Fe atoms. The exchange energies $|2J_{ij}s_is_j|$ are 1.60∼7.10 meV ($r \leq 3.52$ Å) for the former, while the latter are 16.22∼44.6 meV. The temperature dependences of the Bloch and Néel domain walls can also be evaluated by determining the macroscopic parameters, the stiffness constant and magnetic anisotropy constant, from atomistic models. The Monte Carlo method for the canonical ensemble is used to find the domain wall energy $E_{DW}(T)$ at temperature T, and by using a constrained Monte Carlo method with a fixed magnetization direction [48], θ-dependence of the finite temperature magnetic anisotropy energy

$$E_{\mathrm{A}}(T) = K_1(T)\sin^2\theta + K_2(T)\sin^4\theta + K_4(T)\sin^6\theta \quad (20)$$

can be calculated. $K_1(T)$, $K_2(T)$, and $K_4(T)$ for $\mathrm{Nd_2Fe_{14}B}$ are obtained by fitting the coefficients of $E_{\mathrm{A}}(T)$ [13, 17]. The stiffness constant $A(T)$ is obtained by the relation:

$$E_{\mathrm{DW}}(T) = 2\sqrt{A(T)}\int_0^{\pi} d\theta\sqrt{E_{\mathrm{A}}(T)}. \quad (21)$$

From the magnetic anisotropy energy and stiffness constant, the temperature dependence of the domain wall width $dW = \pi\sqrt{\frac{A(T)}{E_{\mathrm{A}}(T)_{\pi/2}-E_{\mathrm{A}}(T)_0}}$ is obtained. The $A(T)$ obtained in this way is actually smaller in the c-axis than in the a-axis, and the temperature dependences of both domain wall widths dW are very close to those in Fig. 5(d) [17].

5. Coercivity of Nanograin

The coercive force (field) is the threshold field at which the metastable magnetization collapses. At absolute zero temperature, it is the field at which the energy barrier vanishes, but at finite temperatures, the process of jumping over the free energy barrier becomes possible due to thermal fluctuations. When the inverse magnetic field is strong or the temperature is high, the barrier disappears and the magnetization relaxes deterministically and smoothly, as shown in Fig. 6(a). On the other hand, when the magnetic field is weak and the temperature is low, there is a barrier as shown in Fig. 6(b), and the relaxation is caused by thermal fluctuations and occurs stochastically as a kind of Poisson process, resulting

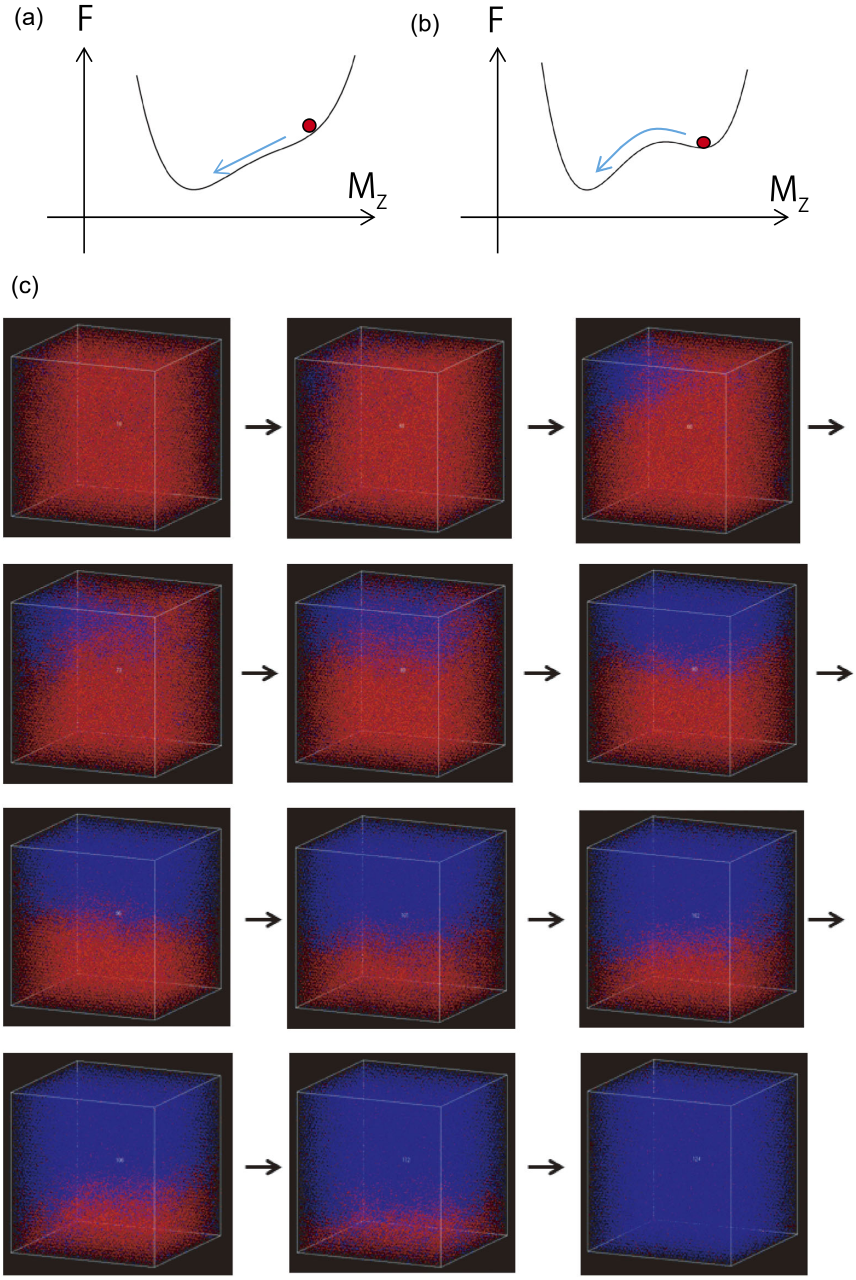

Fig. 6 (a) Deterministic process. (b) Stochastic process by barrier-crossing dynamics. (c) Snapshots of the magnetization reversal for the nano grain from the all-down spin state under a reversed field ($h = 4.0\,\mathrm{T}$). Red and blue parts denote down-spin and up-spin states, respectively. Reprinted figure (c) with permission from [M. Nishino *et al.*, Phys. Rev. B 102, 020413(R) (2020)]. Copyright (2020) by the American Physical Society. (online color) in a longer relaxation time. In this section, we describe methods to investigate the coercivity of nanograins.

The magnetization reversal dynamics by the sLLG method was studied for a nanograin of $12 \times 12 \times 9$ unit cells at $T = 0.46T_{\mathrm{C}}$ (near room temperature) [19]. Figure 6(c) shows snapshots of the magnetization reversal from the down spin state at $\alpha = 0.1$ under the reversed magnetic field $h = 4.0\,\mathrm{T}$. This relaxation is in the stochastic regime. Nucleation occurs from a corner, and the reversal region was first expanded with a Bloch-type domain wall parallel to the *ab*-plane, and then grew in the direction of the *c*-axis with a Néel-type domain wall. This trend is independent of α. This process is due to the fact that the exchange interactions along the *a*- and *b*-axes are stronger than those along the *c*-axis. When a single nucleation is the rate-determining event, the large distribution of relaxation times makes it difficult to evaluate the mean relaxation time. To overcome this difficulty, we introduced a statistical relation between the reversal probability p and the relaxation time τ as a statistical method for evaluating the relaxation time.

If an event (relaxation) occurs with probability p in unit time, the probability that the event occurs for the first time in period $[t, t+\Delta t]$ is $pe^{-pt}\Delta t$. Thus the average relaxation time $\langle\tau\rangle$ is given by the following formula.

$$\langle\tau\rangle = p\int_0^{\infty} te^{-pt}dt = \frac{1}{p}. \qquad (22)$$

The probability that an event occurs in period $[0, t]$ is $P(t) = 1 - e^{-pt}$. Thus, after running N simulations, the number of samples of non magnetization reversal (survived) is $N_{\mathrm{sv}}(t) = N - N_{\mathrm{done}}(t) = Ne^{-pt}$. From this relation, p (and τ) can be obtained from the slope of the graph of $\ln(N_{\mathrm{sv}}(t)/N)$.

Figure 7(a) shows the magnetic field dependence of the relaxation times for various α values. The relaxation time increases rapidly as the magnetic field decreases below 4.2 T. From a real-time simulation of 0.5 ns, a sub-μs relaxation can be calculated by using the statistical relation. Since coercivity is a relaxation phenomenon of 1 s in the experiment, the following fitting function was used to estimate the 1 s relaxation (a long relaxation time). For long relaxation times, a single exponential decay of Arrhenius type is expected. Therefore, the relaxation time was extrapolated by including a correction term in the form of a double exponential fitting of eq. (23).

$$\tau(h) = Ae^{-ah} + Be^{-bh} = Ae^{-ah}(1 + Ce^{-dh}), \qquad (23)$$

where $C = B/A$ and $d = b - a$. In Fig. 7(b), the fitted lines by this equation are depicted. The intersection of each line and $\tau = 1\,\mathrm{s}$ gives the coercive force. The coercive force was estimated to be about 3 T ($H_{\mathrm{c}} = 3$–$3.2\,\mathrm{T}$). From Fig. 7(b), we can see that the threshold field obtained from the realistic simulation time (ns) is about 20–25% larger than the threshold field corresponding to the relaxation of 1 s. In the following sections, we estimate the coercive force from the relaxation of the order of ns, which is about 20% higher than the coercive force corresponding to 1 s.

In the above, we directly measured the relaxation time of magnetization reversal and obtained the relaxation time from $N_{\mathrm{sv}}(t)$, but we can also estimate the coercivity from the survival probability $P(H) = N_{\mathrm{sv}}(H)/N$ for a magnetic field sweep (the field h is denoted by $H(t)$ as a function of time). The probability of Arrhenius relaxation is given by $p = \frac{1}{\tau_0}e^{-\beta E_{\mathrm{B}}(H)}$. For τ_0 we adopt the value $\tau_0 = 10^{-11}\,\mathrm{s}$ [49], which is often used in magnetization reversal. The probability of no relaxation (survival) when the magnetic field is swept from $H = -\infty$ (down spin state) to H as a linear function of time $H(t) = vt$ is given by the following formula [28].

$$P(H) = \exp\left[-\frac{1}{v\tau_0}\int_{-\infty}^{H}\frac{1}{e^{\beta E_{\mathrm{B}}(h)}}dh\right]. \qquad (24)$$

Here, the phenomenological relation often used in the study of magnetization reversal in permanent magnets [50, 51]

$$E_{\mathrm{B}}(H) = E_0\left(1 - \frac{H}{H_0}\right)^n \qquad (25)$$

is applied. E_0 is the energy barrier under zero magnetic field and H_0 is the magnetic field for zero barrier. The value of the exponent n is established as $n = 1{\sim}2$ for many magnetic materials. In the case of coherent magnetization reversal as in the Stoner-Wohlfarth model, the exponent is $n = 2$ [52]. It has been experimentally shown that $n \simeq 1$ in neodymium

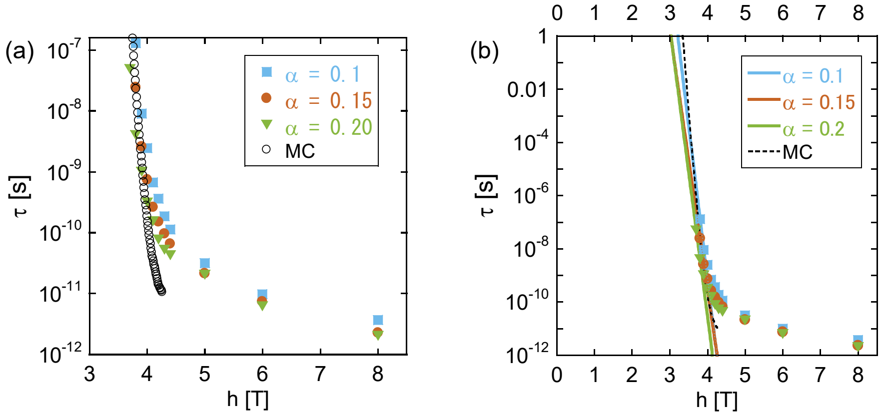

Fig. 7 (a) Magnetic field dependence of the relaxation time (magnetization reversal time) with the damping factor (α) dependence. (b) Extrapolation of the relaxation time. MC denotes the relaxation time of the Arrhenius law ($\tau = \tau_0 e^{\Delta F}$) estimated in a Monte Carlo study [21]. Reprinted figure with permission from [M. Nishino *et al.*, Phys. Rev. B 102, 020413(R) (2020)]. Copyright (2020) by the American Physical Society. (online color) magnets [50, 53]. Here, $n = 1$ is adopted. The above probabilities can also be computed for $n = 2$. In fact, $n = 1$ gives a closer value than $n = 2$ to the coercivity estimated for the above system [28]. Using eq. (25), we obtain

$$\ln(-\ln P(H)) = \frac{\beta E_0}{H_0} H + \ln\left[e^{-\beta E_0} \frac{H_0}{v\tau_0 \beta E_0} \right] \tag{26}$$

and E_0 and H_0 can be evaluated from the slope and y-intercept when the left-hand side is plotted as a function of magnetic field.

On the other hand, the relaxation time τ is $\tau = \tau_0 \exp(\beta \Delta F)$, and from this relation $\beta \Delta F = 25.3$ when $\tau = 1$ s and $\tau_0 = 10^{-11}$ s. Setting $\Delta F = E_{\mathrm{B}}(H)$,

$$\beta \Delta F = \beta E_0 \left(1 - \frac{H_c}{H_0}\right) = 25.3. \tag{27}$$

From this relation, the coercive force is given using H_0 and βE_0 as

$$H_c = H_0 \left(1 - \frac{25.3}{\beta E_0}\right). \tag{28}$$

The coercive force can be calculated using E_0 and H_0 evaluated with the formula (26). In fact, applying this method to the above nanograin, we obtained a coercivity of about 3 T [28].

The coercive force of the nanograin can also be obtained by calculating the free energy for magnetization using the Monte Carlo method described in Sec. 3.1.2. The Wang-Landau method is used to obtain $F(M_z, H = 0)$ under zero magnetic field $H = 0$. The free energy under a magnetic field H is obtained as

$$F(M_z, H) = F(M_z, H = 0) - HM_z. \tag{29}$$

The left panel of Fig. 8(a) shows the relation between the magnetization M_z (M in the figure) and free energy for several magnetic fields including $H = 0$, and the right panel presents the energy barrier at 3.5 T. Figure 8(b) shows energy barriers to the magnetic field for several sizes of grains. Since the energy barrier corresponding to $\beta F = 25.3$ can be crossed by thermally activated effects, the coercive field is the magnetic field at the point where the free energy curve intersects $25.3 k_{\mathrm{B}} T$. In the system of $12 \times 12 \times 9$ unit cells, the intersection of the blue curve and $25.3 k_{\mathrm{B}} T$ is $H_c = 3.3$ T [21]. This value is close to the coercive force obtained by the real-time dynamics method described above, indicating the validity of the coercivity evaluation of both methods. As shown in Fig. 8(b), the coercivity almost saturates when the grain size exceeds 20 nm.

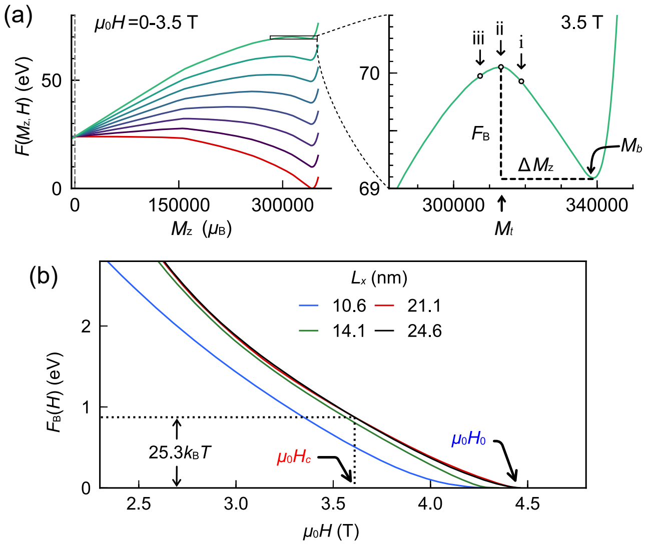

Fig. 8 (a) Free energies as a function of M_z of the $Nd_2Fe_{14}B$ grain at $0.46 T_{\mathrm{C}}$. $L_x = L_y = 14.1$ nm, $L_z = 14.6$ nm. Red line is for $H = 0$ and other lines are for applying H. (b) Free-energy barriers as a function of the magnetic field for four system sizes: $L_x = 10.6$ nm, 14.1 nm, 21.1 nm, 24.6 nm ($L_x = L_y$, $L_z = 1.038 L_x$). Reprinted figure with permission from [Toga *et al.*, npj Comput. Mater. 6, 67 (2020)]. Copyright 2020 NPG. (online color)

6. Nucleation and Pinning Fields

6.1 Hard–soft–hard magnet model

In order to realize stronger coercivity at high temperatures, it is necessary to investigate the effect of grain and grain boundary structures and properties on the coercivity. For this purpose, a hard-soft-hard magnet model (Fig. 9) in which hard magnets are in contact with an intermediate soft magnet has been studied [54–57]. This model captures the essence of nucleation and pinning in inhomogeneous systems and has been used to analyze various phenomena in experimental and theoretical studies of magnetic materials including GMR sensors [50, 58, 59]. In particular, for a continuum model of a hard–soft–hard magnet at zero temperature, one-dimensional nonlinear equations are solved with stiffness and magnetic anisotropy constants as parameters. The obtained diagram representing the nucleation and depinning field thresholds (the former is called nucleation field and the latter pinning field) as a function of the ratio of the parameters is well known and has been used in the interpretation of experiments [55, 56].

Here we will see how the diagram is modified by the effect of thermal fluctuations. For this purpose, we consider a model of hard–soft–hard magnet in a simple cubic lattice of the Heisenberg model with an anisotropy term. First, in order to define the parameters, the continuum model Hamiltonian

$$\mathcal{H} = \int d\boldsymbol{r} \left(\frac{A}{2} (\nabla \boldsymbol{m}(\boldsymbol{r}))^2 - K m_z(\boldsymbol{r})^2 - M \boldsymbol{H} \cdot \boldsymbol{m}(\boldsymbol{r}) \right) \tag{30}$$

is considered. Here, $\boldsymbol{m}$ is the unit vector of the magnetization direction at position $\boldsymbol{r}$, and A is the exchange stiffness constant, K is the anisotropy constant, $\boldsymbol{H}$ is the magnetic field, and M is the magnitude of magnetization. The magnetic

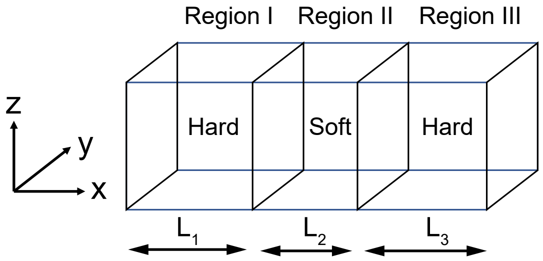

Fig. 9 Schematic picture of a system consisting of two bulk hard magnets and a boundary soft magnet. Regions I and III are characterized by J_1, D_1 and S_1, while region II is characterized by J_2, D_2 and S_2. Free boundary conditions are adopted for the lattice model. (online color)

properties of the hard (soft) magnets are specified by the stiffness constant A_1 (A_2), the anisotropy constant K_1 (K_2), and the magnitude of magnetization M_1 (M_2). Normalized external magnetic field

$$h = \frac{H}{H_{\mathrm{SW}}}, \quad H_{\mathrm{SW}} \equiv \frac{2K_1}{M_1} \tag{31}$$

and parameters

$$F = \frac{A_2 M_2}{A_1 M_1} \tag{32}$$

$$E = \frac{A_2 K_2}{A_1 K_1}, \tag{33}$$

are defined [12, 55]. H_{SW} is the Stoner-Wohlfarth field of the hard magnets.

Consider the case where the magnetization of the system is oriented in the positive direction (z direction) and a reversed magnetic field is applied. The state of magnetization in each of the regions I to III is defined as follows.

- $(+++)$ is a state in which the magnetizations in regions I, II, and III are in the positive direction.
- $(+-+)$ is a state in which nucleation and then magnetization reversal have occurred in region II, while the magnetizations in the other regions remain positive.
- $(+--)$ is a state where the magnetization is kept without reversal only in region I.
- $(---)$ is a state where the magnetizations in the whole region are reversed.

The threshold field at which $(+++) \rightarrow (+-+)$ occurs at $T = 0$, i.e., the threshold field at which nucleation occurs in region II (soft phase) is given by

$$h_{\mathrm{NCII}}(0) = \frac{E}{F}. \tag{34}$$

However, this is calculated in the limit of infinite width of W, and the threshold value is slightly larger than this value when W is of finite width [55]. The threshold field at which $(+-+) \rightarrow (---)$ or $(+--) \rightarrow (---)$ occurs at $T = 0$, i.e., the threshold field at which the domain wall propagates from region II to regions I and III (hard magnet phase) is given by

$$h_{\mathrm{DWP}}(0) = \frac{1-E}{(1+\sqrt{F})^2}. \tag{35}$$

This magnetic field is called the pinning field. For $h < h_{\mathrm{DWP}}(0)$, the domain wall does not propagate into the hard magnetic phase. For $h_{\mathrm{NCII}}(0) < h < h_{\mathrm{DWP}}(0)$, the magnetization reversed by nucleation is confined to region II and the state is $(+-+)$. For the magnetization reversal of the whole system, the threshold field (nucleation field) is the larger value of $h_{\mathrm{NCII}}(0)$ and $h_{\mathrm{DWP}}(0)$,

$$h_{\mathrm{NC}}(0) = \max\left[\frac{E}{F}, \frac{1-E}{(1+\sqrt{F})^2}\right]. \tag{36}$$

The dotted line (straight line) in Fig. 10(a) illustrates this relation for $F = 0.5$.

In the following, we treated the anisotropic Heisenberg model on the lattice (37) to investigate temperature effects [12]. We observed how this diagram changes with temperature effects. The system is the following spin model on a simple cubic lattice with $L_x \times L_y \times L_z = 60 \times 6 \times 6$ sites. $L_1 = L_2 = L_3 = 20$.

$$\mathcal{H} = -\sum_{\langle i,j \rangle} J_{i,j} \boldsymbol{s}_i \cdot \boldsymbol{s}_j - \sum_{i=1}^{N} D_i S_{i,z}^2 - H \sum_{i=1}^{N} S_{i,z}. \tag{37}$$

For $J_{i,j} > 0$, only the nearest neighbor interaction was considered, and $g\mu_{\mathrm{B}} = 1$ was the unit.

In this case, J was used instead of A, D instead of K, and the parameters F and E were defined as

$$F = \frac{J_2 S_2}{J_1 S_1}, \tag{38}$$

$$E = \frac{J_2 D_2}{J_1 D_1}. \tag{39}$$

The magnitudes of magnetization were set equal in regions I, II, and III ($|\boldsymbol{S}_i| = S_1 = S_2 = 1$) and the magnetic anisotropy energy of the hard phase was set to $D_1 = 0.2J_1$. The Curie temperature of the hard phase is $T_{\mathrm{C}} \simeq 1.5J_1$. Here, for the magnetic field, we used the normalized field $h = H/H_{\mathrm{SW}}$ as in eq. (31). Here, $H_{\mathrm{SW}} = 2D_1/S_1$.

Using the sLLG method, we simulated the time evolution of the states by applying a reversed magnetic field to the $(+++)$ state and investigated the magnetic field thresholds.

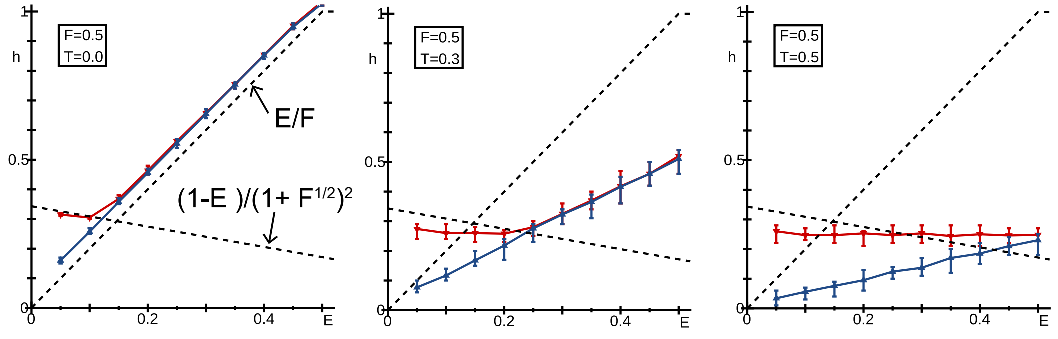

(a) (b) (c)

Fig. 10 Threshold fields between $(+++)$ and $(+-+)$ (blue upward triangles) and between $(+-+)$ and $(---)$ (red downward triangles) for $F = 0.5$ at (a) $T = 0$, (b) $T = 0.3J_1$, and (c) $T = 0.5J_1$. The dotted lines denote $h_{\mathrm{NCII}}(0)$ in (34) and $h_{\mathrm{DWP}}(0)$ in (35). Reprinted figure with modification from [S. Mohakud *et al.*, Phys. Rev. B 94, 054430 (2016)]. Copyright (2016) by the American Physical Society. (online color)

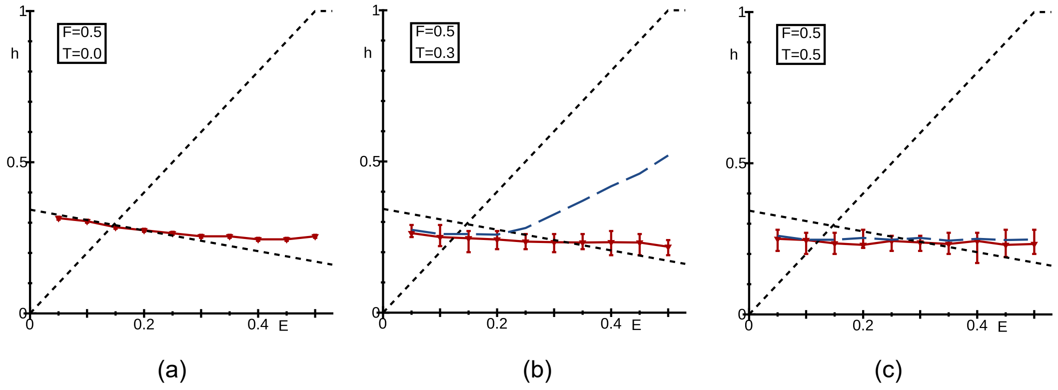

Fig. 11 Threshold fields between $(+--)$ and $(---)$ (red downward triangles) for $F=0.5$ at (a) $T=0$, (b) $T=0.3J_1$, and (c) $T=0.5J_1$. Blue dashed lines denote threshold fields between $(+-+)$ and $(---)$ in Fig. 10. Reprinted figure with permission from [S. Mohakud *et al.*, Phys. Rev. B 94, 054430 (2016)]. Copyright (2016) by the American Physical Society. (online color)

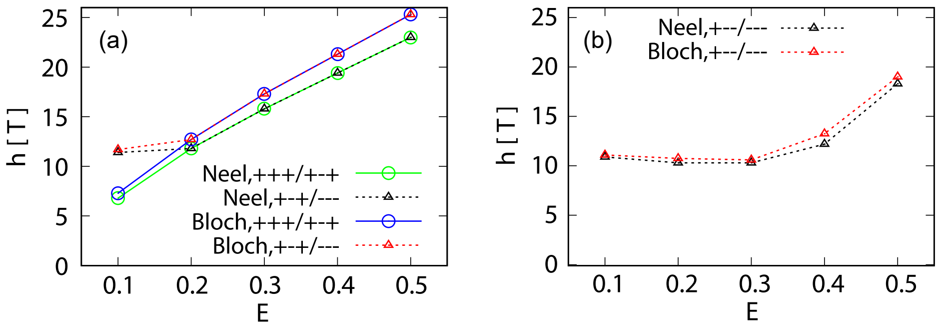

Fig. 12 (a) Threshold fields at 0 K between $(+++)$ and $(+-+)$ (circles) and between $(+-+)$ and $(---)$ (triangles) with the comparison between Bloch and Néel domain walls. (b) Threshold fields at 0 K between $(+--)$ and $(---)$ with the comparison between Bloch and Néel domain walls. Reprinted figure with permission from [I.E. Uysal *et al.*, Phys. Rev. B 101, 094421 (2020)]. Copyright (2020) by the American Physical Society. (online color)

Figure 10(a) shows the magnetic field thresholds for $(+++)\to(+-+)$ (blue line) and $(+-+)\to(---)$ (red line) at $T=0$. It can be seen that the analytical value for the continuum model (dotted line) is a good approximation. Figure 11(a) gives the threshold field of $(+--)\to(---)$ at $T=0$. In this case, the magnetic field thresholds for small E coincide with the analytical values of the continuum model, but for large E, the magnetic field thresholds shift upward from the analytical values. This is due to the so-called narrow domain wall effect, which makes the continuum approximation poor [12]. As seen in Figs. 10(b) and 10(c), the field thresholds of $(+++)\to(+-+)$ and $(+-+)\to(---)$ decrease significantly from the field thresholds of $T=0$ as the temperature increases, and the $(+-+)$ region expands. As shown in Figs. 11(b) and 11(c), the threshold field of $(+--)\to(---)$ also decreases due to the temperature effect, but the E dependence becomes moderate. Especially in the narrow domain wall situation, the magnetization state of regions II and III has little influence on region I, and the surface nucleation in region I becomes important [12].

6.2 Nucleation and pinning fields in $Nd_2Fe_{14}B$

The nucleation and pinning fields were evaluated for the cases of Bloch and Néel walls, respectively, by simulating a hard-soft-hard magnet model composed of the atomistic model (4) of $Nd_2Fe_{14}B$ [20]. In the case of Bloch wall, the a direction corresponds to the x direction in Fig. 9, and the c direction to the x direction in the case of Néel wall. The soft magnet phase (grain boundary) is complex with an amorphous-like structure that depends on experimental conditions. Since the first-principles study [60, 61] has just begun and it is difficult to use the microscopic parameters established at this time, we assumed the same structure as the hard magnet phase. The parameters E and F are defined as in the previous section. However, in $Nd_2Fe_{14}B$, there are various kinds of exchange interactions and magnetic anisotropy energies, which were scaled in the same proportion. Figure 12(a) shows for the Bloch and Néel domain walls the E-dependences of the threshold field between $(+++)$ and $(+-+)$ and between $(+-+)$ and $(---)$ at $T=0$ K. We assumed $F=0.5$. $L_1=L_2=L_3=12$ unit cells and the height and depth are 5 unit cells. The outline of the diagram is similar to that of the anisotropic Heisenberg model described in the previous section. The threshold field is lower in the case of the Néel wall, reflecting the weaker exchange interaction in the c-axis. Figure 12(b) exhibits the threshold field between $(+--)$ and $(---)$ at $T=0$ K. This pinning field is not so different between the two domain walls as in the case of the nucleation field. Where E is large, the threshold value increases reflecting the nature of the narrow down wall.

Figure 13(a) depicts the magnetic field thresholds between $(+++)$ and $(+-+)$ and between $(+-+)$ and $(---)$ at $T=0.34T_C$, and Fig. 13(b) shows the threshold field between $(+--)$ and $(---)$. Compared with the change of the threshold field between $T=0$ and $T=0.5J_1$

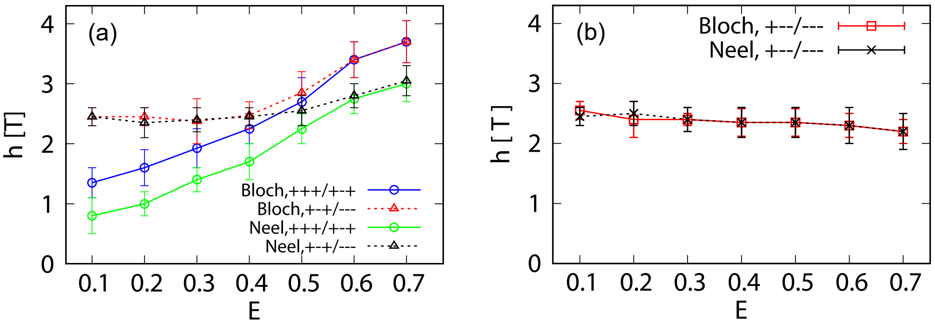

Fig. 13 (a) Threshold fields at $0.34T_C$ between $(+++)$ and $(+-+)$ (circles) and between $(+-+)$ and $(---)$ (triangles) with the comparison between Bloch and Néel domain walls. (b) Threshold fields at $0.34T_C$ between $(+--)$ and $(---)$ with the comparison between Bloch and Néel domain walls. Reprinted figure with permission from [I.E. Uysal *et al.*, Phys. Rev. B 101, 094421 (2020)]. Copyright (2020) by the American Physical Society. (online color)

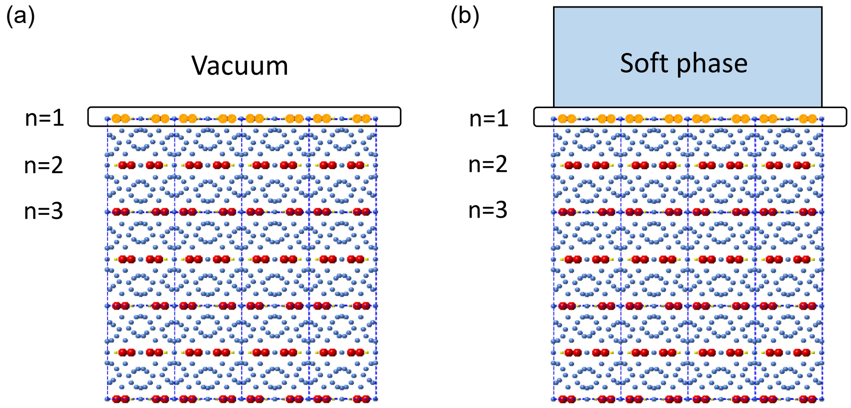

Fig. 14 (a) System A. The Nd surface layers were in contact with vacuum. In this example, Nd atoms (red) in the first Nd layer were substituted by Dy atoms (orange). The Nd layers are numbered as $n = 1, 2, \cdots$. (b) System B. The Nd surface layers were in contact with a soft magnet phase. [M. Nishino *et al.*, Phys. Rev. B 106, 054422 (2022)]. Copyright (2022) by the American Physical Society. (online color)

($\simeq 0.33T_C$) for $F = 0.5$ in the anisotropic Heisenberg model of the previous section, the threshold field of $Nd_2Fe_{14}B$ shows a larger decrease rate due to temperature effects. This is may be due to the sensitiveness to temperature effects because of the weaker exchange interaction between Nd and Fe compared to that between Fe and due to the property of the magnetic anisotropy energy of Nd, which is the origin of the spin rearrangement transition.

7. Dysprosium Substitution Effect

As mentioned in the introduction, Nd magnets have problems in high-temperature properties and are often substituted with Dy to suppress the decrease in coercive force at high temperatures. Experiments using the method of grain boundary diffusion process have shown that the coercivity can be enhanced without loosing remanence [62–66]. Dy-rich shells have been observed to form between the grain boundary and core grains [66]. The effect of this coercivity enhancement by Dy substitution has been studied by micromagnetics calculations using macroscopic parameters of the Dy-substituted phase [67, 68]. The enhancement effect at absolute zero temperature has also been investigated in a simplified crystal lattice model [69]. However, the microscopic origin of the coercivity-enhancing effect of Dy substitution, including the temperature effect, can be understood only by the method of atomistic modeling.

Here we explain the mechanism and effect of the coercivity enhancement by Dy substitution based on an atomistic model [27]. The Hamiltonian (4) has the energy term of the crystal electric field of eq. (40).

$$\mathcal{H} = \sum_{i}^{\text{Nd,Dy}} \sum_{l,m} \Theta_{l,i} A_{l,i}^{m} \langle r^{l} \rangle_{i} \hat{O}_{l,i}^{m} \qquad (40)$$

is composed of Nd and Dy atoms. For Dy, the coefficients of the crystal electric field, etc. are those of Dy. For Dy atoms, $J = \mathcal{L} + \mathcal{S} = 15/2$ and $g_T = 4/3$. As shown in Fig. 2(b), $\boldsymbol{s}_i$ of Dy atoms and $\boldsymbol{S}_i$ ($= \boldsymbol{s}_i$) of Fe atoms are antiferromagnetically coupled. The magnitude of this exchange interaction is almost the same as that between Nd and Fe atoms [27]. In this case, unlike Fig. 2(a), $\boldsymbol{S}_i$ ($= \boldsymbol{s}_i + \mathcal{J}_i$) of a Dy atom and $\boldsymbol{S}_i$ ($= \boldsymbol{s}_i$) of an Fe atom are antiferromagnetically coupled.

As shown in Fig. 14, the Nd layers are numbered from $n = 1$ at the (001) surface of the hard magnet phase of $Nd_2Fe_{14}B$ to $n = 2$ and $n = 3 \cdots$ toward the interior. We considered two systems: the system in Fig. 14(a) where the surface is in contact with the vacuum (system A) and the system in Fig. 14(b) where the surface is in contact with the soft magnet phase (system B). The hard magnet phase consists of $12 \times 12 \times 9$ unit cells, the soft magnet phase $12 \times 12 \times 3$ unit cells, with periodic boundary conditions in the *a* and *b* axes, and a free boundary condition for system A and periodic boundary condition for system B in the *c* axis. Here, all Nd atoms from layer 1 to layer *n* were replaced by

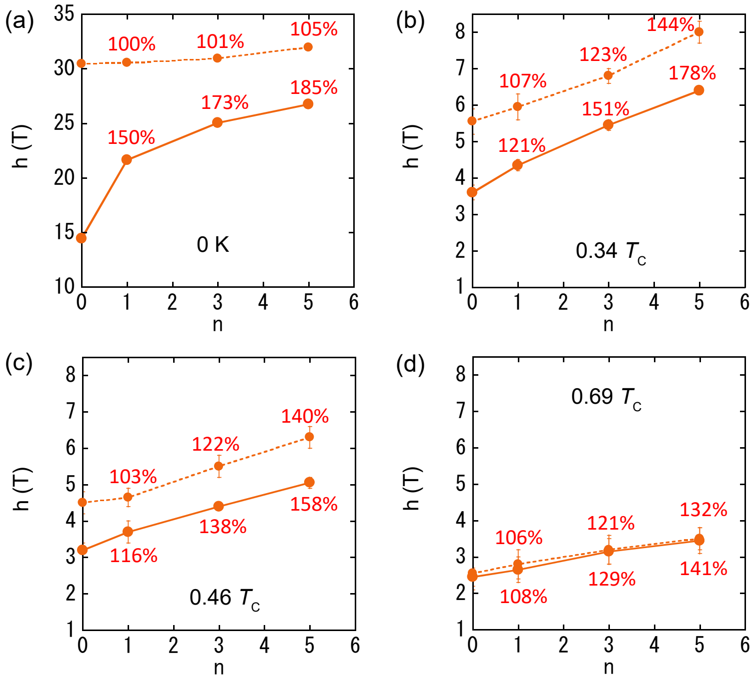

Fig. 15 *n* dependence of the threshold filed in systems A (dotted lines) and B (solid lines) at (a) 0 K, (b) $0.34T_C$, (c) $0.46T_C$, and (d) $0.69T_C$. Reprinted figure with permission from [M. Nishino *et al.*, Phys. Rev. B 106, 054422 (2022)]. Copyright (2022) by the American Physical Society. (online color)

Dy atoms, and the threshold field of magnetization reversal was investigated. As in the previous section, the soft magnet phase was assumed to have the same structure as the hard magnet phase, and small magnetic parameters (exchange interactions by a factor of 0.5 and magnetic anisotropy energies by a factor of 0.2) were adopted as in the micromagnetics calculations. The threshold field of magnetization reversal was estimated by real-time simulation of the sLLG method.

Figure 15 presents the *n* dependence of the threshold field and its temperature dependence for system A (dotted line) and system B (solid line). $n = 0$ means no Dy substitution (original system). The ratios (%) in the figures are those against the value of $n = 0$. Since magnetization reversal occurs more easily in the grain boundary phase, domain walls are more easily generated at the phase boundary, and surface nucleation of the hard magnet phase tends to occur. Therefore, the coercive force is greatly reduced compared to that of the vacuum surface. However, the ratio against $n = 0$ when *n* increases in system B is larger than that in system A, and the coercive force increases by a large ratio with Dy substitution in system B. In other words, the enhancement of coercivity is more intensely in system B. This is a characteristic feature of Dy substitution, and it suggests that Dy substitution has a strong pinning effect hindering the domain wall motion to the hard magnet phase. The rate of increase of coercivity ($\Delta h_C/\Delta n$) with respect to the number of Dy substitution layers (*n*) is constant at finite temperature and almost equal for both systems.

Regarding system A, we investigated *n*-dependence of the coercivity for the system with the magnetic anisotropy of Nd atoms enhanced by a factor of 2 instead of Dy substitution [22], and compared it with that of Dy substitution. We compared the ratios of increase of $n = 5$ against $n = 0$ for $0.34T_C$, $0.46T_C$, and $0.69T_C$. In the case of Dy-substitution, the increase is 144%, 140%, and 132%, respectively, while in the case of doubly enhanced magnetic anisotropy of Nd atoms, the increase is 123%, 121%, and 111% [22]. This indicates that the coercivity enhancement effect is maintained at high temperatures in the case of Dy substitution.

Next, we observed at the change in nucleation dynamics when the substituted Dy layer was increased. Figure 16 shows the nucleation of $n = 1$ and $n = 5$ in system B. The magnetic field was used near the threshold value. Figure 16(a) shows the case with $n = 1$ where only one layer was Dy-substituted. A large part of the soft magnet phase was reversed before the magnetization of the hard magnet phase was reversed, indicating that depinning occurs from the surface of the hard magnet phase. On the other hand, Fig. 16(b) has five Dy-substituted layers and nucleation occurred from the inside of the hard magnet part. Surface nucleation is suppressed by Dy substitution, and is replaced by bulk nucleation. This change in nucleation mechanism was also observed in system A, but *n* boundary for the change from surface nucleation to internal nucleation was $n \simeq 2$ in system A and $n \simeq 3$ in system B.

There are two possible microscopic origins of the coercivity enhancement effect of Dy substitution and its maintenance at high temperatures. The first is the difference in magnetic interactions. The interaction between Nd and Fe atoms is ferromagnetic, while that between Dy and Fe is antiferromagnetic. This antiferromagnetic coupling stabilizes the Dy moment under the reversed magnetic field and prevents nucleation for reversal. The second is the feature of the temperature dependence of the CEF energy of Dy. Figure 4(b) depicts the temperature dependence of the CEF energy of Dy atoms in the Nd magnet. Compared with Fig. 4(a), the CEF energy of Dy atoms has a minimum at

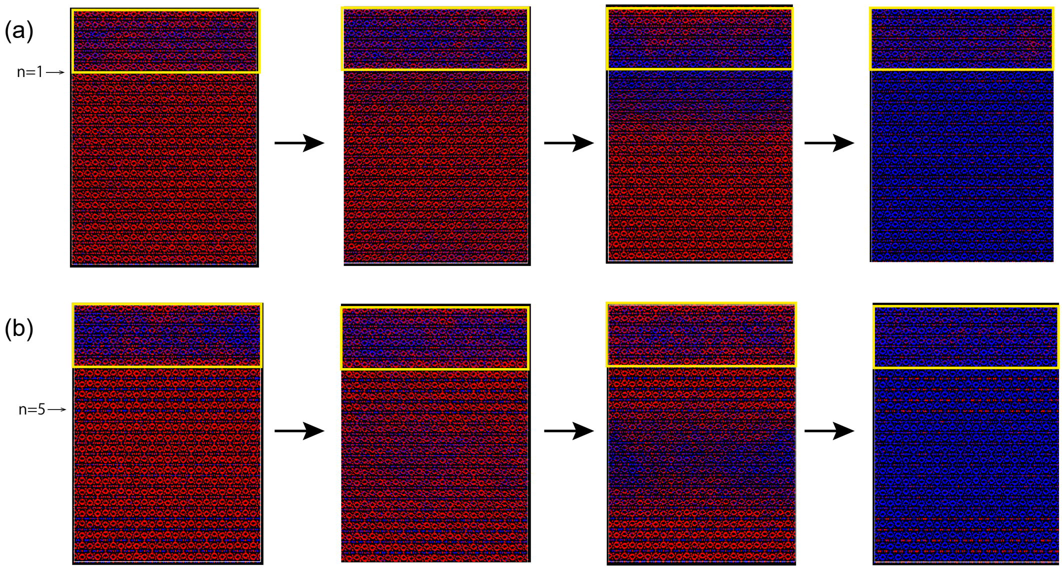

Fig. 16 Snapshots of the spin configuration in nucleation for (a) $n = 1$ and (b) $n = 5$ at the threshold fields $h = 3.70\,\mathrm{T}$ and $h = 5.05\,\mathrm{T}$, respectively, at $0.46T_\mathrm{C} \simeq T_\mathrm{room}$ in system B. The yellow-boxed regions correspond to the soft magnetic phase. Red and blue parts denote up-spin and down-spin ones, respectively. Reprinted figure with permission from [M. Nishino *et al.*, Phys. Rev. B 106, 054422 (2022)]. Copyright (2022) by the American Physical Society. (online color)

$\theta = 0$ regardless of temperature, and the potential barrier is relatively high at all temperatures. Furthermore, when we focus on the change of the potential barrier between $0.46T_\mathrm{C}$ (near room temperature) and $0.69T_\mathrm{C}$, we find that the potential barrier of Dy is 27% higher than that of Nd at $0.46T_\mathrm{C}$, but is 79% higher at $0.69T_\mathrm{C}$. In other words, Dy has a relatively higher potential barrier at high temperatures. This may be the reason why Dy substitution is effective at high temperatures.

8. Magnetic Dipole Interaction

Since the atomistic model method takes into account the spins of all atoms, the computable scale is realistically limited to the order of tens of nm. The magnetic dipole interaction is much smaller than the exchange interaction and is not very important at that scale. Therefore, the magnetic dipole interaction

$$\frac{1}{4\pi\mu_0}\sum_{i\neq k}\frac{1}{r_{ik}^3}\left(\boldsymbol{S}_i\cdot\boldsymbol{S}_k-\frac{3(\boldsymbol{r}_{ik}\cdot\boldsymbol{S}_i)(\boldsymbol{r}_{ik}\cdot\boldsymbol{S}_k)}{r_{ik}^2}\right) \tag{41}$$

has not been taken into account, but it becomes important at the scale of an assembly of grains (μm) because of the appearance of uniform magnetization in ferromagnets. The demagnetization field effect given by this interaction has the effect of breaking the uniform order, and experiments and micromagnetic calculations have shown a decrease in coercivity (increase in demagnetization field effect) with respect to grain size [70–73]. The coercivity of nanograins shown in this paper (saturation at about 20 nm) is considered to give an approximation of the upper limit of the coercivity including the effect of thermal fluctuations of grain assembly. The exchange interaction is of short range and the computational cost of the simulation is proportional to the spin number N, while the magnetic dipole interaction is of long range and thus it increases with the square of the spin number (N^2). In Monte Carlo methods, the stochastic cutoff (SCO) and other methods have been proposed to overcome this difficulty [74, 75]. The SCO method accelerates the calculation by reducing the selectivity of long-range weak interactions in a state-update process of the Monte Carlo method while maintaining the detailed balance condition and ensuring that the simulation reaches equilibrium correctly as a steady state. For a 3-dimensional system of magnetic dipole interactions, a single Monte Carlo step can be computed in $O(N\ln N)$ time. However, the conventional SCO method has difficulties that make the procedure cumbersome for systems with complex unit cells such as Nd magnets, but a modified SCO method (MSCO) using Walker's algorithm has been developed and the effect of magnetic dipole interaction has been investigated in a thin film system of an atomistic model of Nd [15]. In addition, magnetic profiles have been studied using MSCO for a simple anisotropic Heisenberg model with parameters of anisotropy constant, dipole interaction, and system thickness [26].

9. Summary and Future Perspective

This paper introduces the methodologies for studying the effects of temperature and thermal fluctuations on the magnetic properties of permanent magnets and describes the magnetic properties obtained by applying the methodologies, especially focusing on the properties of neodymium magnets. The method of the atomistic model introduced here is an extension of the study of thermal fluctuation effects initiated by Brown [76], and correctly treats entropy effects and temperature effects including local thermal fluctuations in many-body systems of spins with cooperative interactions. In this paper, we first presented a modeling of the interaction from the atomic level in $\mathrm{Nd_2Fe_{14}B}$. Then, the characteristics of magnetization process, domain wall, coercivity of nanograin, nucleation and pinning fields, and dysprosium substitution effect were explained using Monte Carlo and sLLG methods. There, the understanding of thermal fluctuations and temperature effects and their microscopic mechanisms in the magnetic properties of permanent magnets, which had not been well understood, was advanced, as seen in the significant decrease in coercive force due to thermal fluctuations.

Although we did not mention them due to space limitation, the angular dependence of nucleation and pinning fields and the effect of the orientation distribution of magnetic anisotropy of grains are also important for coercivity studies, and studies of their finite temperature properties have been started using the above methodologies [77]. A nontrivial behavior in the temperature dependence of the ferromagnetic resonance of neodymium magnets has also been clarified by the method of atomistic modeling [18].

The magnetization reversal of individual grains has been observed experimentally, and the effect of thermal fluctuations on the process has become a realistic problem [78]. Therefore, the rigorous treatment of thermal fluctuations and temperature effects by this atomistic model is expected to become more and more important in the future. In fact, during the ESICMM project, European and Chinese groups have also started to study the atomistic model of $\mathrm{Nd_2Fe_{14}B}$ [79–83], and the study of permanent magnets using this approach is expected to be developed hereafter. However, when using the atomistic model, the current computing power is limited to calculations on the scale of a few tens of nm. This is the range in which a single grain or a few grains can be included. Coercivity appears as a property of an assembly of grains. The assembly of grains requires calculations on the order of µm, which is done in micromagnetics calculations.

If we start from an atomistic model and obtain macroscopic $A(T)$ and $K(T)$ using the constraint Monte Carlo method introduced in 4.2, the LLG calculation for micromagnetics cannot handle thermal activation processes. Adding a noise field for thermal fluctuations leads to a double temperature effect, which is inappropriate. Therefore, it is necessary to develop a methodology that starts from an atomistic model and connects it to the µm order scale. For this purpose, it is necessary to construct a coarse-grained model consisting of local spin variables that incorporates the effects of thermal fluctuations. For example, the following method can be considered. For a spin set in a certain region, we introduce a coarse-grained magnetization $\boldsymbol{M}$. The magnitude of this coarse-grained magnetization is variable due to temperature effects, and the magnetization distribution $P(\boldsymbol{M})$ can be calculated by the Wang-Landau method using an atomistic model. For this coarse-grained magnetization, we construct a coarse-grained Hamiltonian.

$$\mathcal{H} = -\sum_{i,j} J_{i,j} \boldsymbol{M}_i \cdot \boldsymbol{M}_j + \sum_i E_{\mathrm{self}}(\boldsymbol{M}_i), \tag{42}$$

where $E_{\mathrm{self}}(\boldsymbol{M}_i)$ is the magnetic anisotropy energy and other contributions. The renormalized parameters ($J_{i,j}$, etc.) are adjusted to reproduce the values of physical quantities obtained in the original atomistic Hamiltonian. It is conceivable to apply this coarse-grained Hamiltonian to large systems, including magnetic dipole interactions. The details are under investigation.

Acknowledgements

The study presented here was supported by the Elements Strategy Initiative Center for Magnetic Materials (ESICMM) (project number JPMXP0112101004) funded by the Ministry of Education, Culture, Sports, Science and Technology (MEXT) of Japan. This paper is the result of collaborative researches with Satoshi Hirosawa, Ismail Enes Uysal, Hiroshi Hayasaka, Yuta Toga, Taichi Hinokihara, Sasmita Mohakud, Sergio Andraus, Munehisa Matsumoto, Shotaro Doi, Hisazumi Akai, Akimasa Sakuma and Takashi Miyake. We would like to take this opportunity to express our deepest gratitude to them. We also thank the other ESICMM members for helpful discussions.

REFERENCES

[1] M. Sagawa and S. Hirosawa: Magnetic hardening mechanism in sintered R–Fe–B permanent magnets, J. Mater. Res. **3** (1988) 45–54.
[2] S. Hirosawa, Y. Matsuura, H. Yamamoto, S. Fujimura, M. Sagawa and H. Yamauchi: Single Crystal Measurements of Anisotropy Constants of $\mathrm{R_2Fe_{14}B}$ (R=Y, Ce, Pr, Nd, Gd, Tb, Dy and Ho), Jpn. J. Appl. Phys. **24** (1985) L803.
[3] J.F. Herbst: $\mathrm{R_2Fe_{14}B}$ materials: Intrinsic properties and technological aspects, Rev. Mod. Phys. **63** (1991) 819–898.
[4] S. Hirosawa, Y. Matsuura, H. Yamamoto, S. Fujimura, M. Sagawa and H. Yamauchi: Magnetization and magnetic anisotropy of $\mathrm{R_2Fe_{14}B}$ measured on single crystals, J. Appl. Phys. **59** (1986) 873–879.
[5] A.V. Andreev, A.V. Deryagin, N.V. Kudrevatykh, N.V. Mushnikov, V.A. Reimer and S.V. Terent'ev: MAGNETIC PROPERTIES OF $\mathrm{Y_2FE_{14}B}$ AND $\mathrm{ND_2FE_{14}B}$ AND THEIR HYDRIDES, Sov. Phys. JETP **63** (1986) 608–612.
[6] O. Yamada, Y. Ohtsu, F. Ono, M. Sagawa and S. Hirosawa: Magnetocrystalline anisotropy in $\mathrm{Nd_2Fe_{14}B}$ intermetallic compound, J. Magn. Magn. Mater. **70** (1987) 322–324.
[7] X.C. Kou, R. Grössinger, G. Hilscher, H.R. Kirchmayr and F.R. de Boer: ac susceptibility study on $R_2\mathrm{Fe_{14}B}$ single crystals ($R =$ Y, Pr, Nd, Sm, Gd, Tb, Dy, Ho, Er, Tm), Phys. Rev. B **54** (1996) 6421–6429.
[8] C. Piqué, R. Burriel and J. Bartolomé: Spin reorientation phase transitions in $\mathrm{R_2Fe_{14}B}$ (R = Y, Nd, Ho, Er, Tm) investigated by heat capacity measurements, J. Magn. Magn. Mater. **154** (1996) 71–82.
[9] S. Hirosawa, M. Nishino and S. Miyashita: Perspectives for high-performance permanent magnets: applications, coercivity, and new materials, Adv. Nat. Sci.: Nanosci. Nanotechnol. **8** (2017) 013002.
[10] S. Hirosawa: Magune **17** (2022) 175–180.
[11] M. Nishino and S. Miyashita: Realization of the thermal equilibrium in inhomogeneous magnetic systems by the Landau-Lifshitz-Gilbert equation with stochastic noise, and its dynamical aspects, Phys. Rev. B **91** (2015) 134411.
[12] S. Mohakud, S. Andraus, M. Nishino, A. Sakuma and S. Miyashita: Temperature dependence of the threshold magnetic field for nucleation and domain wall propagation in an inhomogeneous structure with grain boundary, Phys. Rev. B **94** (2016) 054430.
[13] Y. Toga, M. Matsumoto, S. Miyashita, H. Akai, S. Doi, T. Miyake and A. Sakuma: Monte Carlo analysis for finite-temperature magnetism of $\mathrm{Nd_2Fe_{14}B}$ permanent magnet, Phys. Rev. B **94** (2016) 174433.
[14] M. Nishino, Y. Toga, S. Miyashita, H. Akai, A. Sakuma and S. Hirosawa: Atomistic-model study of temperature-dependent domain walls in the neodymium permanent magnet $\mathrm{Nd_2Fe_{14}B}$, Phys. Rev. B **95** (2017) 094429.
[15] T. Hinokihara, M. Nishino, Y. Toga and S. Miyashita: Exploration of the effects of dipole-dipole interactions in $\mathrm{Nd_2Fe_{14}B}$ thin films based on a stochastic cutoff method with a novel efficient algorithm, Phys. Rev. B **97** (2018) 104427.
[16] S. Miyashita, M. Nishino, Y. Toga, T. Hinokihara, T. Miyake, S. Hirosawa and A. Sakuma: Perspectives of stochastic micromagnetism of $\mathrm{Nd_2Fe_{14}B}$ and computation of thermally activated reversal process, Scr. Mater. **154** (2018) 259–265.
[17] Y. Toga, M. Nishino, S. Miyashita, T. Miyake and A. Sakuma:

Anisotropy of exchange stiffness based on atomic-scale magnetic properties in the rare-earth permanent magnet $Nd_2Fe_{14}B$, Phys. Rev. B **98** (2018) 054418.

[18] M. Nishino and S. Miyashita: Nontrivial temperature dependence of ferromagnetic resonance frequency for spin reorientation transitions, Phys. Rev. B **100** (2019) 020403(R).

[19] M. Nishino, I.E. Uysal, T. Hinokihara and S. Miyashita: Dynamical aspects of magnetization reversal in the neodymium permanent magnet by a stochastic Landau-Lifshitz-Gilbert simulation at finite temperature: Real-time dynamics and quantitative estimation of coercive force, Phys. Rev. B **102** (2020) 020413(R).

[20] I.E. Uysal, M. Nishino and S. Miyashita: Magnetic field threshold for nucleation and depinning of domain walls in the neodymium permanent magnet $Nd_2Fe_{14}B$, Phys. Rev. B **101** (2020) 094421.

[21] Y. Toga, S. Miyashita, A. Sakuma and T. Miyake: Role of atomic-scale thermal fluctuations in the coercivity, npj Comput. Mater. **6** (2020) 67.

[22] M. Nishino, I.E. Uysal and S. Miyashita: Effect of the surface magnetic anisotropy of neodymium atoms on the coercivity in neodymium permanent magnets, Phys. Rev. B **103** (2021) 014418.

[23] M. Nishino, I.E. Uysal, T. Hinokihara and S. Miyashita: Finite-temperature dynamical and static properties of Nd magnets studied by an atomistic modeling, AIP Adv. **11** (2021) 025102.

[24] S. Miyashita, M. Nishino, Y. Toga, T. Hinokihara, I.E. Uysal, T. Miyake, H. Akai, S. Hirosawa and A. Sakuma: Atomistic theory of thermally activated magnetization processes in $Nd_2Fe_{14}B$ permanent magnet, Sci. Technol. Adv. Mater. **22** (2021) 658–682.

[25] S. Miyashita, M. Nishino, Y. Toga, T. Hinokihara, I.E. Uysal, T. Miyake, H. Akai, S. Hirosawa and A. Sakuma: Atomistic Theory of Thermally Activated Magnetization Processes in $Nd_2Fe_{14}B$ Permanent Magnet, J. Jpn. Soc. Powder Powder Metallurgy **69** (2022) S126–S146.

[26] T. Hinokihara and S. Miyashita: Systematic survey of magnetic configurations in multilayer ferromagnet system with dipole-dipole interaction, Phys. Rev. B **103** (2021) 054421.

[27] M. Nishino, H. Hayasaka and S. Miyashita: Microscopic origin of coercivity enhancement by dysprosium substitution into neodymium permanent magnets, Phys. Rev. B **106** (2022) 054422.

[28] M. Nishino and S. Miyashita: submitted.

[29] H. Kronmüllar and M. Fähnle: *Micromagnetism and the Microstructure of Ferromagnetic Solids*, (Cambridge University Press, 2003).

[30] J.F. Herbst, J.J. Croat, F.E. Pinkerton and W.B. Yelon: Relationships between crystal structure and magnetic properties in $Nd_2Fe_{14}B$, Phys. Rev. B **29** (1984) 4176–4178.

[31] A.I. Liechtenstein, M.I. Katsnelson, V.P. Antropov and V.A. Gubanov: Local spin density functional approach to the theory of exchange interactions in ferromagnetic metals and alloys, J. Magn. Magn. Mater. **67** (1987) 65–74.

[32] Y. Miura, H. Tsuchiura and T. Yoshioka: Magnetocrystalline anisotropy of the Fe-sublattice in $Y_2Fe_{14}B$ systems, J. Appl. Phys. **115** (2014) 17A765.

[33] M. Yamada, H. Kato, H. Yamamoto and Y. Nakagawa: Crystal-field analysis of the magnetization process in a series of $Nd_2Fe_{14}B$-type compounds, Phys. Rev. B **38** (1988) 620–633.

[34] A.J. Freeman and R.E. Watson: Theoretical Investigation of Some Magnetic and Spectroscopic Properties of Rare-Earth Ions, Phys. Rev. **127** (1962) 2058–2075.

[35] J.L. García-Palacios and F.J. Lázaro: Langevin-dynamics study of the dynamical properties of small magnetic particles, Phys. Rev. B **58** (1998) 14937–14958.

[36] H. Suwa and S. Todo: Markov Chain Monte Carlo Method without Detailed Balance, Phys. Rev. Lett. **105** (2010) 120603.

[37] B. Berg and T. Neuhaus: Multicanonical ensemble: A new approach to simulate first-order phase transitions, Phys. Rev. Lett. **68** (1992) 9–12.

[38] F. Wang and D.P. Landau: Efficient, Multiple-Range Random Walk Algorithm to Calculate the Density of States, Phys. Rev. Lett. **86** (2001) 2050–2053.

[39] K. Hukushima and K. Nemoto: Exchange Monte Carlo Method and Application to Spin Glass Simulations, J. Phys. Soc. **65** (1996) 1604–1608.

[40] B.A. Berg, U. Hansmann and T. Neuhaus: Simulation of an ensemble with varying magnetic field: A numerical determination of the order-order interface tension in the $D=2$ Ising model, Phys. Rev. B **47** (1993) 497–500.

[41] K. Watanabe and M. Sasaki: An Efficient Monte-Carlo Method for Calculating Free Energy in Long-Range Interacting Systems, J. Phys. Soc. Jpn. **80** (2011) 093001.

[42] K. Binder: Finite size scaling analysis of ising model block distribution functions, Z. Phys. B **43** (1981) 119–140.

[43] M. Sagawa, S. Fujimura, H. Yamamoto, Y. Matsuura, S. Hirosawa and K. Hiraga: Proceedings of the 4th International Symposium on Magnetic Anisotropy and Coercivity in Rare Earth Transition Metal Alloys, ed. by K.J. Strnat, (University of Dayton, Dayton, OH, 1985) p. 587 and Coercivity in Rare Earth Transition Metal Alloys, ed. by K.J. Strnat, (University of Dayton, Dayton, OH, 1985) p. 587.

[44] K. Ono, N. Inami, K. Saito, Y. Takeichi, M. Yano, T. Shoji, A. Manabe, A. Kato, Y. Kaneko, D. Kawana, T. Yokoo and S. Itoh: Observation of spin-wave dispersion in Nd-Fe-B magnets using neutron Brillouin scattering, J. Appl. Phys. **115** (2014) 17A714.

[45] Y. Zhu and M.R. McCartney: Magnetic-domain structure of $Nd_2Fe_{14}B$ permanent magnets, J. Appl. Phys. **84** (1998) 3267–3272.

[46] S.J. Lloyd, J.C. Loudon and P.A. Midgley: Measurement of magnetic domain wall width using energy-filtered Fresnel images, J. Microscopy **207** (2002) 118–128.

[47] M. Beleggia, M.A. Schofield, Y. Zhu and G. Pozzi: Quantitative domain wall width measurement with coherent electrons, J. Magn. Magn. Mater. **310** (2007) 2696–2698.

[48] P. Asselin, R.F.L. Evans, J. Barker, R.W. Chantrell, R. Yanes, O. Chubykalo-Fesenko, D. Hinzke and U. Nowak: Constrained Monte Carlo method and calculation of the temperature dependence of magnetic anisotropy, Phys. Rev. B **82** (2010) 054415.

[49] D. Givord, A. Lienard, P. Tenaud and T. Viadieu: Magnetic viscosity in Nd-Fe-B sintered magnets, J. Magn. Magn. Mater. **67** (1987) L281–L285.

[50] S. Okamoto, R. Goto, N. Kikuchi, O. Kitakami, T. Akiya, H. Sepehri-Amin, T. Ohkubo, K. Hono, K. Hioki and A. Hattori: Temperature-dependent magnetization reversal process and coercivity mechanism in Nd-Fe-B hot-deformed magnets, J. Appl. Phys. **118** (2015) 223903.

[51] W. Wernsdorfer, E.B. Orozco, K. Hasselbach, A. Benoit, B. Barbara, N. Demoncy, A. Loiseau, H. Pascard and D. Mailly: Experimental Evidence of the Néel-Brown Model of Magnetization Reversal, Phys. Rev. Lett. **78** (1997) 1791–1794.

[52] R.H. Victora: Predicted time dependence of the switching field for magnetic materials, Phys. Rev. Lett. **63** (1989) 457–460.

[53] S. Okamoto: Experimental approaches for micromagnetic coercivity analysis of advanced permanent magnet materials, Sci. Technol. Adv. Mater. **22** (2021) 124–134.

[54] R. Friedberg and D.I. Paul: New Theory of Coercive Force of Ferromagnetic Materials, Phys. Rev. Lett. **34** (1975) 1234–1237.

[55] A. Sakuma, S. Tanigawa and M. Tokunaga: Micromagnetic studies of inhomogeneous nucleation in hard magnets, J. Magn. Magn. Mater. **84** (1990) 52–58.

[56] A. Sakuma: The theory of inhomogeneous nucleation in uniaxial ferromagnets, J. Magn. Magn. Mater. **88** (1990) 369–375.

[57] A.L. Wysocki and V.P. Antropov: Micromagnetic simulations with periodic boundary conditions: Hard-soft nanocomposites, J. Magn. Magn. Mater. **428** (2017) 274–286.

[58] T. Pramanik, A. Roy, R. Dey, A. Rai, S. Guchhait, H.C.P. Movva, C.-C. Hsieh and S.K. Banerjee: Angular dependence of magnetization reversal in epitaxial chromium telluride thin films with perpendicular magnetic anisotropy, J. Magn. Magn. Mater. **437** (2017) 72–77.

[59] Y. Feng, J. Liu, T. Klein, K. Wu and J.-P. Wang: Localized detection of reversal nucleation generated by high moment magnetic nanoparticles using a large-area magnetic sensor, J. Appl. Phys. **122** (2017) 123901.

[60] Y. Tatetsu, S. Tsuneyuki and Y. Gohda: First-Principles Study of the Role of Cu in Improving the Coercivity of Nd-Fe-B Permanent Magnets, Phys. Rev. Appl. **6** (2016) 064029.

[61] Y. Gohda, Y. Tatetsu and S. Tsuneyuki: Electron Theory on Grain-Boundary Structures and Local Magnetic Properties of Neodymium Magnets, Mater. Trans. **59** (2018) 332–337.

[62] K. Hirota, H. Nakamura, T. Minowa and M. Honshima: Coercivity Enhancement by the Grain Boundary Diffusion Process to Nd–Fe–B Sintered Magnets, IEEE Trans. Magn. **42** (2006) 2909–2911.

[63] F. Xu, J. Wang, X. Dong, L. Zhang and J. Wu: Grain boundary

microstructure in DyF_3-diffusion processed Nd–Fe–B sintered magnets, J. Alloy. Compd. **509** (2011) 7909–7914.

[64] K. Löewe, C. Brombacher, M. Katter and O. Gutfleisch: Temperature-dependent Dy diffusion processes in Nd–Fe–B permanent magnets, Acta Mater. **83** (2015) 248–255.

[65] W. Chen, J.M. Luo, Y.W. Guan, Y.L. Huang, M. Chen and Y.H. Hou: Grain boundary diffusion of Dy films prepared by magnetron sputtering for sintered Nd–Fe–B magnets, J. Phys. D **51** (2018) 185001.

[66] T.-H. Kim, T. Sasaki, T. Ohkubo, Y. Takada, A. Kato, Y. Kaneko and K. Hono: Microstructure and coercivity of grain boundary diffusion processed Dy-free and Dy-containing Nd–Fe–B sintered magnets, Acta Mater. **172** (2019) 139–149.

[67] S. Bance, J. Fischbacher, A. Kovacs, H. Oezelt, F. Reichel and T. Schrefl: Thermal Activation in Permanent Magnets, JOM **67** (2015) 1350–1356.

[68] J. Fischbacher, A. Kovacs, L. Exl, J. Kuhnel, E. Mehofer, H. Sepehri-Amin, T. Ohkubo, K. Hono and T. Schrefl: Searching the weakest link: Demagnetizing fields and magnetization reversal in permanent magnets, Scr. Mater. **154** (2018) 253–258.

[69] C. Mitsumata, H. Tsuchiura and A. Sakuma: Model Calculation of Magnetization Reversal Process of Hard Magnet in $Nd_2Fe_{14}B$ System, Appl. Phys. Express **4** (2011) 113002.

[70] S. Bance, B. Seebacher, T. Schrefl, L. Exl, M. Winklhofer, G. Hrkac, G. Zimanyi, T. Shoji, M. Yano, N. Sakuma, M. Ito, A. Kato and A. Manabe: Grain-size dependent demagnetizing factors in permanent magnets, Appl. Phys. **116** (2014) 233903.

[71] R. Ramesh, G. Thomas and B.M. Ma: Magnetization reversal in nucleation controlled magnets. II. Effect of grain size and size distribution on intrinsic coercivity of Fe-Nd-B magnets, J. Appl. Phys. **64** (1988) 6416–6423.

[72] K. Uestuener, M. Katter and W. Rodewald: Dependence of the Mean Grain Size and Coercivity of Sintered Nd–Fe–B Magnets on the Initial Powder Particle Size, IEEE Trans. Magn. **42** (2006) 2897–2899.

[73] T. Fukada, M. Matsuura, R. Goto, N. Tezuka, S. Sugimoto, Y. Une and M. Sagawa: Evaluation of the Microstructural Contribution to the Coercivity of Fine-Grained Nd–Fe–B Sintered Magnets, Mater. Trans. **53** (2012) 1967–1971.

[74] M. Sasaki and F. Matsubara: Stochastic Cutoff Method for Long-Range Interacting Systems, J. Phys. Soc. Jpn. **77** (2008) 024004.

[75] K. Fukui and S. Todo: Order-N cluster Monte Carlo method for spin systems with long-range interactions, J. Comput. Phys. **228** (2009) 2629–2642.

[76] W.F. Brown, Jr.: Thermal Fluctuations of a Single-Domain Particle, Phys. Rev. **130** (1963) 1677–1686.

[77] H. Hayasaka, M. Nishino and S. Miyashita: Microscopic study on the angular dependence of coercivity at zero and finite temperatures, Phys. Rev. B **105** (2022) 224414.

[78] T. Yomogita, S. Okamoto, N. Kikuchi, O. Kitakami, H. Sepehri-Amin, Y.K. Takahashi, T. Ohkubo, K. Hono, K. Hioki and A. Hattori: Direct detection and stochastic analysis on thermally activated domain-wall depinning events in micropatterned Nd-Fe-B hot-deformed magnets, Acta Mater. **201** (2020) 7–13.

[79] Q. Gong, M. Yi, R.F.L. Evans, B.-X. Xu and O. Gutfleisch: Calculating temperature-dependent properties of $Nd_2Fe_{14}B$ permanent magnets by atomistic spin model simulations, Phys. Rev. B **99** (2019) 214409.

[80] Q. Gong, M. Yi and B.-X. Xu: Multiscale simulations toward calculating coercivity of Nd-Fe-B permanent magnets at high temperatures, Phys. Rev. Mater. **3** (2019) 084406.

[81] Q. Gong, M. Yi, R.F.L. Evans, O. Gutfleisch and B.-X. Xu: Anisotropic exchange in Nd–Fe–B permanent magnets, Mater. Res. Lett. **8** (2020) 89–96.

[82] S.C. Westmoreland, R.F.L. Evans, G. Hrkac, T. Schrel, G.T. Zimanyi, M. Winklhofer, N. Sakuma, M. Yano, A. Kato, T. Shoji, A. Manabe, M. Ito and R.W. Chantrell: Multiscale model approaches to the design of advanced permanent magnets, Scr. Mater. **148** (2018) 56–62.

[83] S.C. Westmoreland, C. Skelland, T. Shoji, M. Yano, A. Kato, M. Ito, G. Hrkac, T. Schrefl, R.F.L. Evans and R.W. Chantrell: Atomistic simulations of α-Fe/$Nd_2Fe_{14}B$ magnetic core/shell nanocomposites with enhanced energy product for high temperature permanent magnet applications, J. Appl. Phys. **127** (2020) 133901.